JGR Solid Earth

RESEARCH ARTICLE
10.1029/2020JB019885

Key Points:
- Longmaxi formation shales show a strong variation in mineral composition due to the different depositional environments
- A small proportion of phyllosilicate-poor gouges exhibit velocity weakening at hydrothermal conditions, indicative of potentially unstable slip
- Aseismic fault slip during hydraulic fracturing may reactivate adjacent and distal unstable faults and trigger the seismicity

Supporting Information:
- Supporting Information S1

Correspondence to:
F. Zhang,
fengshou.zhang@tongji.edu.cn

Citation:
An, M., Zhang, F., Elsworth, D., Xu, Z., Chen, Z., & Zhang, L. (2020). Friction of Longmaxi shale gouges and implications for seismicity during hydraulic fracturing. *Journal of Geophysical Research: Solid Earth*, *125*, e2020JB019885. https://doi.org/10.1029/2020JB019885

Received 10 APR 2020
Accepted 20 JUL 2020
Accepted article online 22 JUL 2020

Friction of Longmaxi Shale Gouges and Implications for Seismicity During Hydraulic Fracturing

Mengke An[1,2], Fengshou Zhang[1,2], Derek Elsworth[3,4], Zhengyu Xu[5], Zhaowei Chen[6], and Lianyang Zhang[7]

[1]Department of Geotechnical Engineering, College of Civil Engineering, Tongji University, Shanghai, China, [2]Key Laboratory of Geotechnical and Underground Engineering of Ministry of Education, Tongji University, Shanghai, China, [3]Department of Energy and Mineral Engineering, EMS Energy Institute and G3 Center, Pennsylvania State University, University Park, PA, USA, [4]Department of Geosciences, Pennsylvania State University, University Park, PA, USA, [5]PetroChina Hangzhou Institute of Geology, Hangzhou, China, [6]CNPC Engineering Technology R&D Company Limited, Beijing, China, [7]Department of Civil and Architectural Engineering and Mechanics, University of Arizona, Tucson, AZ, USA

Abstract Longmaxi formation shales are the major target reservoir for shale gas extraction in Sichuan Basin, southwest China. Swarms of earthquakes accompanying hydraulic fracturing are observed at depths typifying the Longmaxi formation. Mineral composition varies broadly through the stratigraphic section due to different depositional environments. The section is generally tectosilicate-poor and phyllosilicate-rich with a minor portion the converse. We measure the frictional and stability properties of shale gouges taken from the full stratigraphic section at conditions typifying the reservoir depth. Velocity-stepping experiments were performed on representative shale gouges at a confining pressure of 60 MPa, pore fluid pressure of 30 MPa, and temperature of 150°C. Results show the gouges are generally frictionally strong with friction coefficients ranging between 0.50 and 0.75. Two phyllosilicate + TOC (total organic carbon)-poor gouges exhibited higher frictional strength and velocity weakening, capable of potentially unstable fault slip, while only velocity strengthening was observed for the remaining phyllosilicate + TOC-rich gouges. These results confirm that the frictional and stability properties are mainly controlled by phyllosilicate + TOC content. Elevating the temperature further weakens the gouges and drives it toward velocity weakening. The presence of observed seismicity in a majority of velocity-strengthening materials suggests the importance of the velocity-weakening materials. We suggest a model where seismicity is triggered when pore fluid pressures drive aseismic slip and triggers seismic slip on adjacent faults in the same formation and distant faults in the formations above/below. The effect of pore pressure transients within low-permeability shale gouges is incorporated. Our results highlight the importance of understanding mechanisms of induced earthquakes and characterizing fault properties prior to hydraulic fracturing.

1. Introduction

Induced seismicity has become a major concern during the recovery of unconventional resources, including shale gas extraction, enhanced geothermal system (EGS) and carbon dioxide (CO_2) sequestration (Kim et al., 2018; Majer et al., 2007; Shapiro et al., 2006; Suckale, 2009; Walsh & Zoback, 2015). The injection of large volumes of fluid into the subsurface can reactivate preexisting faults and trigger seismicity (Bao & Eaton, 2016; Ellsworth et al., 2013; Rubinstein & Mahani, 2015). Understanding the physics of injection-induced earthquakes is vital to mitigate the hazard.

In China, the Sichuan Basin (Figure 1) possesses a rich shale gas resource and has become an important area for shale gas production (Liang et al., 2012; Zou et al., 2016). The Changning and Weiyuan national shale gas demonstration areas (Figure 1) in the southwestern Sichuan Basin have experienced an increasing number of earthquakes since the initiation of hydraulic fracturing for reservoir stimulation. Swarms of $M_L \geq 0$ earthquakes have occurred in Changning, Gongxian, Xingwen, and Junlian counties in the Changning national shale gas demonstration area and in Weiyuan and Rongxian counties and Zizhong City in the Weiyuan national shale gas demonstration area at depths of 2–3 km (Figures 2a and 2b). The drilling of horizontal wells in the Changning and Weiyuan areas was initiated in 2011, but systematic hydraulic fracturing for

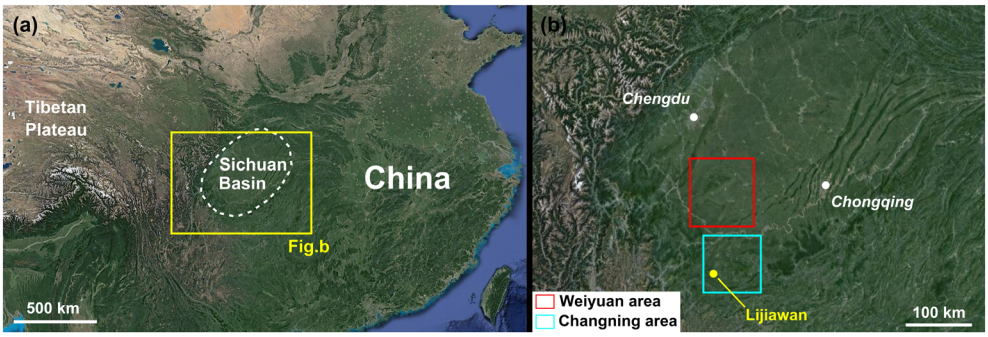

Figure 1. (a) Location of the Sichuan Basin (dashed white circle). Sichuan Basin is located to the east of the Tibetan Plateau and in the southwest of China. The yellow rectangle indicates the area of Panel b. (b) Location of the Changning (coordinates: 104.25–105.33°E, 27.83–28.75°N) and Weiyuan (coordinates: 104.0–105.2°E, 28.9–30.0°N) national shale gas demonstration areas in the southern Sichuan Basin. Both figures were derived from Google Maps. Cyan and red inserts in (b) reference the areas of Figures 2a and 2b, respectively. White solid circles are the cities of Chengdu and Chongqing with the shales collected from Lijiawan Village (yellow solid circle).

shale gas exploitation in those horizontal wells started in 2014 (Lei et al., 2017). Based on the data provided by the China Earthquake Networks Center, the number of $M_L \geq 0$ earthquakes at 2–3 km depth increased from ~300 in 2013 to ~850 in 2015, to ~1,750 in 2017, and then to ~3,000 in September 2019, in the Changning area (Figure 2c). Event growth was even more rapid in the Weiyuan area (Figure 2d), growing from ~10 in 2013 to ~650 in 2015, to ~1,650 in 2017, and then finally to ~3,500 in September 2019. This dramatic increase in earthquake rate correlates with an increased intensity in hydraulic fracturing. The largest earthquake magnitude was M_L ~ 3.7 in the Changning area (June 2019) and M_L ~ 3.3 in the Weiyuan area (September 2019) (Figures 2e and 2f). The target reservoirs for both these areas are in the Longmaxi Formation shales at 2–3 km depth (Chen et al., 2014; Liu et al., 2013). Understanding the frictional and stability properties of these Longmaxi shales can provide insight into the mechanisms controlling the increase in seismicity and potentially provide information to mitigate its occurrence.

With the growth in shale gas recovery, more attention has been applied to understanding the frictional and stability properties of shale fault gouges and fractures that are implicated in injection-induced seismicity (Fang et al., 2017; Jia et al., 2019; Kohli & Zoback, 2013; Scuderi & Collettini, 2018; Shen et al., 2019; Zhang et al., 2019). These studies have identified relationships between mineral composition and the frictional characteristics of shale gouges/fractures in a variety of experimental configurations and boundary conditions (e.g., applied stresses, humidity, and shear velocities). These results highlight the important influence of phyllosilicate contents in lowering the frictional strength but in stabilizing the deformation of shale gouges under the condition of room temperature. However, temperature is known to both change gouge composition via chemical reactions and accelerate fluid-assisted chemical processes (den Hartog et al., 2012; He et al., 2016)—and such characterizations for Longmaxi shale, implicated in recent injection-induced seismicity, are absent. The net thickness of the Longmaxi formation ranges from tens to hundreds of meters in southwest China (Jiang et al., 2016; Xu et al., 2019) and comprises a heterogeneous distribution of different mineralogies. Whether friction and stability vary with either stratigraphic unit or depth is unknown. The following study systematically explores these aspects under hydrothermal conditions to better understand possible mechanisms for induced and triggered earthquakes in the Changning and Weiyuan areas of China.

Three hypotheses potentially address triggering mechanisms of seismicity associated with fluid injection, as illustrated in Figure 3. The first model attributes the fault reactivation to the direct impact fluid injection into the fault (Bao & Eaton, 2016; Ellsworth et al., 2013; Garagash & Germanovich, 2012; Rubinstein & Mahani, 2015), reducing strength and promoting failure. This model requires a high permeability pathway between the reservoir and faults or for the injection well to directly transect the subsurface faults. The second model considers a change in fault loading conditions resulting from poroelastic stress transfer (Deng et al., 2016; Ellsworth et al., 2013, 2016; Eyre et al., 2019; Segall & Lu, 2015) where direct permeation into the fault is not required. Such events are often observed during waste water disposal and may be delayed due to the small magnitude of the poroelastic stress and its diminishment with distance. A third model

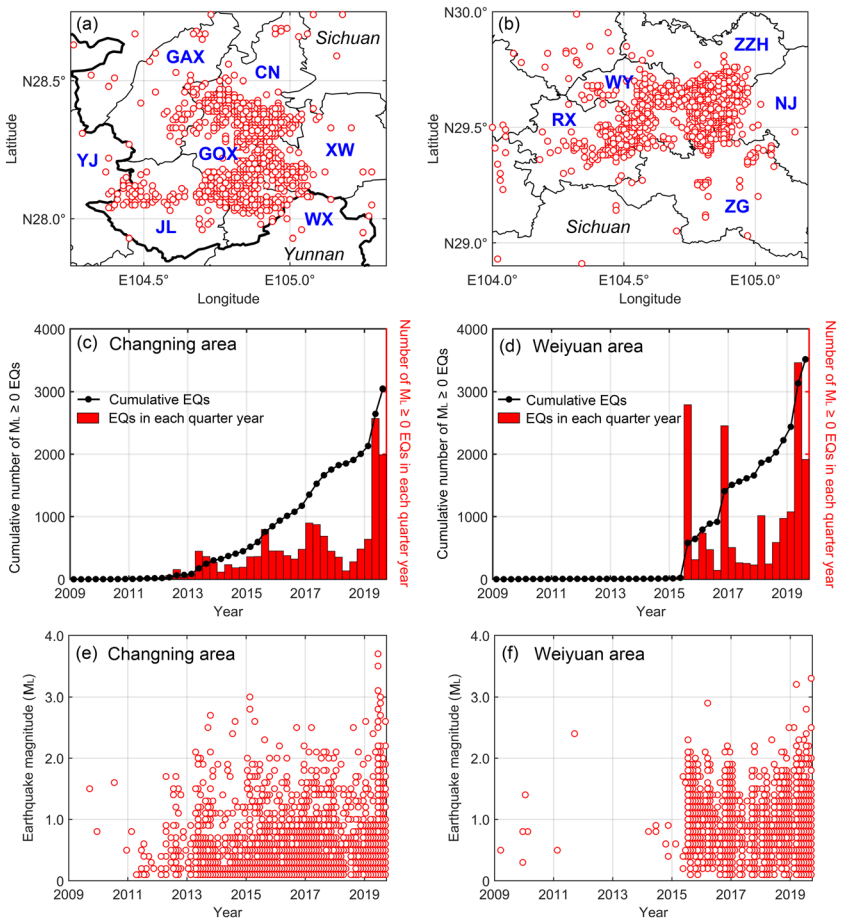

Figure 2. Distribution of $M_L \geq 0$ earthquakes (EQs) in the (a) Changning and (b) Weiyuan areas in the depth interval of 2–3 km from January 2009 to September 2019. Red circles denote $M_L \geq 0$ EQs. Thin solid lines in (a) and (b) represent county boundaries, and the bold black solid line represents the provincial boundaries (Sichuan Province and Yunnan Province). Blue typeface in (a) and (b) indicate county or (city) names: GAX = Gaoxian, CN = Changning, GOX = Gongxian, XW = Xingwen, JL = Junlian, YJ = Yanjin, WY = Weiyuan, ZZH = Zizhong, RX = Rongxian, NJ = Neijiang (city), and ZG = Zigong (city). Cumulative number of $M_L \geq 0$ EQs and number of $M_L \geq 0$ EQs in each quarter year in the (c) Changning and (d) Weiyuan areas from January 2009 to September 2019. EQs of magnitude of $M_L \geq 0$ in the (e) Changning and (f) Weiyuan areas from January 2009 to September 2019. The EQ data are derived online (from www.data.earthquake.cn).

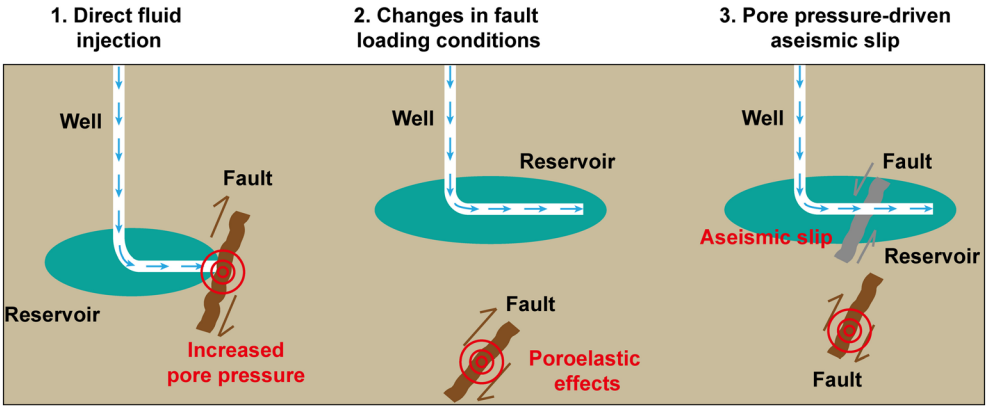

Figure 3. Schematic of potential mechanisms for induced earthquakes (after Ellsworth et al., 2013; Eyre et al., 2019).

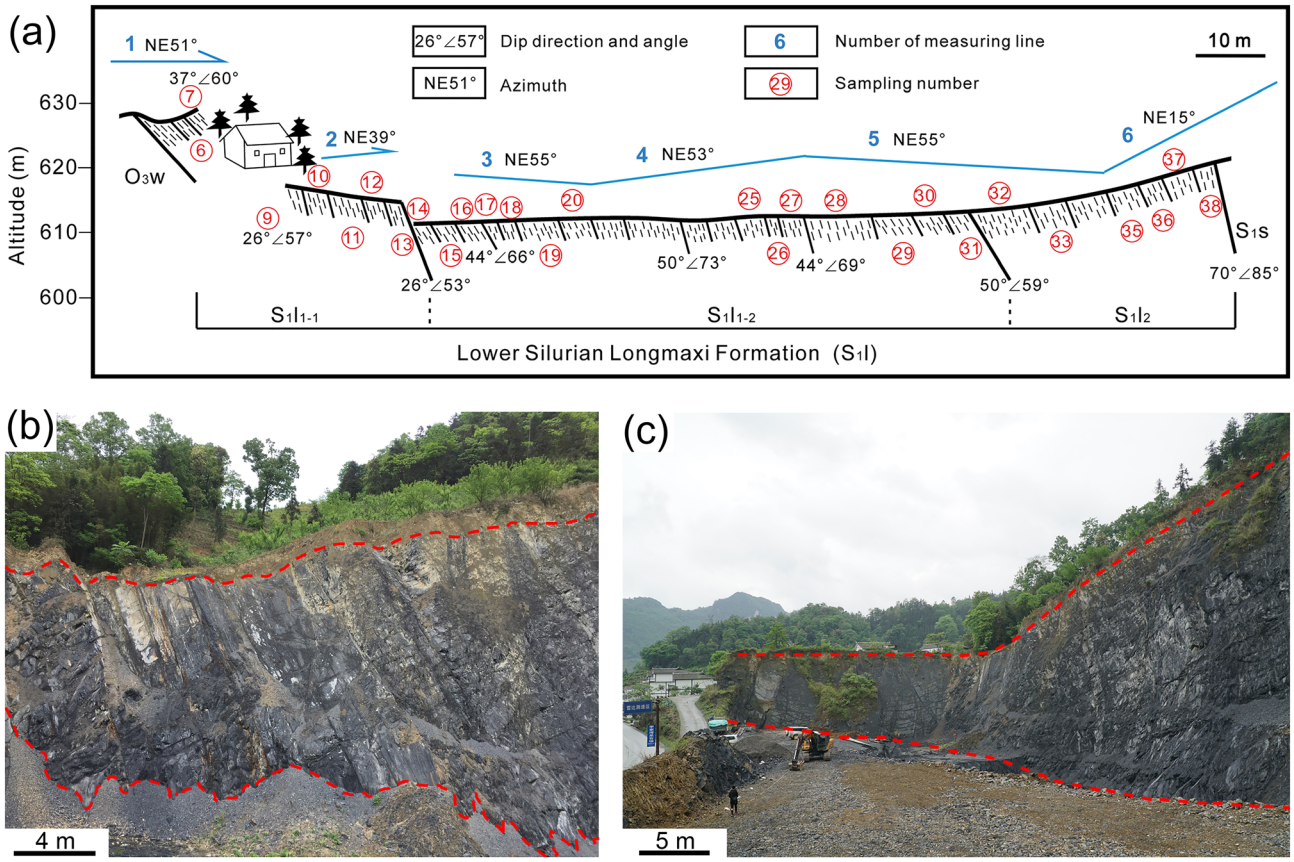

Figure 4. (a) Schematic showing the geologic section and shale sampling locations (samples: 6#–38#) at Lijiawan Village, Niuzhai Township, Yanjin County, Zhaotong City, Yunnan Province. Samples run from the base (6#) to the top (38#) of the stratigraphic section. The location of Lijiawan is shown in Figure 1. The geologic section covers the Upper Ordovician Wufeng formation (O_3w), Lower Silurian Longmaxi formation (S_1l), and Lower Silurian Shiniulan formation (S_1s), with a total section thickness of ~160 m. The Longmaxi formation (S_1l) is divided into two subsections, that is, sections Long 1 (S_1l_1) and Long 2 (S_1l_2). The Long 1 section is further subdivided into two further subsections defined as Subsections Long 1-1 ($S_1l_{1\text{-}1}$) and Long 1-2 ($S_1l_{1\text{-}2}$). (b and c) The outcrop exposures of the Longmaxi shale represented in the geologic section.

posits that earthquakes are triggered by pore fluid pressure-driven aseismic slip (Bhattacharya & Viesca, 2019; Cappa et al., 2019; Eyre et al., 2019; Guglielmi et al., 2015; Scuderi & Collettini, 2016) that may reactivate fault slip in remote and unpressurized regions. The widespread distribution of earthquakes in the Changning and Weiyuan areas (Figure 2), remote from direct injection, suggests that the remote triggering of the second and third models may be an attractive model—one that potentially invokes aseismic slip as an enabling mechanism.

In the following we (1) determine the mineralogic compositions of the Lower Silurian Longmaxi formation shales and (2) link this to the frictional strength and stability of these shale reservoir gouges at hydrothermal conditions. We use these data to (3) determine potential mechanisms of fault reactivation driven by aseismic fault slip during hydraulic fracturing. A full stratigraphic sequence of Longmaxi formation shales was recovered from a geologic section in Lijiawan Village, Niuzhai Township, Yanjin County, Zhaotong City, Yunnan Province (coordinates: 104°26′33.9″E, 28°07′55.4″N), near the Changning area (Figure 4 and supporting information Figure S1). The Longmaxi shale samples from the outcrop at Lijiawan Village were deposited in the same geological period (Lower Silurian) as the shale samples in the Changning and Weiyuan national shale gas demonstration areas and are representative of the two areas (Tan et al., 2014; Zou et al., 2010). The Longmaxi shales are exposed at the surface close to Lijiawan Village due to several polycyclic tectonic movements in the Sichuan Basin (Guo, 2013). The stratigraphic column (Figure S1) shows that the formations above and below the Longmaxi formation are Lower Silurian Shiniulan and Upper Ordovician Wufeng formations, respectively. The Linxiang formation is located below the Wufeng formation. The lithology in the Wufeng formation is the same as Longmaxi formation, but limestone dominates the Shiniulan and Linxiang

Table 1
Mineral Compositions (wt.%) and TOC Contents (wt.%) of All Collected Shales Samples

Shale samples	6#	7#	9#	10#	11#	12#	13#	14#	15#	16#	17#	18#	19#	20#	25#	26#	27#	28#	29#	30#	31#	32#	33#	35#	36#	37#	38#
Quartz	61.8	68.0	49.5	53.0	46.0	28.4	31.3	30.4	34.9	31.5	31.6	29.7	31.8	29.7	26.8	24.0	24.8	24.7	21.8	28.8	22.0	24.9	23.8	17.9	22.9	20.0	4.0
Albite	6.8	5.0	8.6	7.7	14.0	14.7	15.7	12.8	16.9	12.8	12.9	12.8	13.9	9.9	7.9	8.0	5.9	6.9	7.9	6.9	6.0	7.0	5.0	6.0	5.0	7.0	6.0
Orthoclase	3.9	3.0	3.8	3.9	6.0	4.9	5.9	5.9	4.0	6.9	6.9	6.9	5.9	4.0	3.0	3.0	3.0	2.0	5.0	3.0	5.0	3.0	2.0	2.0	2.0	5.0	3.0
Calcite	—	—	—	—	—	10.7	10.8	9.8	10.0	12.8	10.9	8.9	7.9	9.9	20.8	22.0	26.7	24.8	28.8	14.9	38.0	31.9	39.8	51.8	47.8	43.0	79.3
Dolomite	—	—	—	—	—	2.9	2.9	6.9	9.0	3.0	4.0	4.0	—	—	—	3.0	4.0	3.0	3.0	—	—	—	—	—	—	—	—
Pyrite	—	—	—	—	—	2.0	2.0	2.0	6.0	2.0	2.0	2.0	2.0	3.9	2.0	2.0	2.0	2.0	2.0	3.0	—	—	—	—	—	2.0	1.0
Illite	19.8	22.3	29.3	25.7	30.3	17.0	17.3	16.2	8.3	16.3	15.3	18.3	21.0	23.7	22.8	23.6	20.6	20.3	17.2	22.2	20.3	23.7	18.2	18.2	17.7	14.3	3.6
Kaolinite	—	—	—	—	—	—	—	—	2.1	—	—	—	—	—	—	—	—	—	—	—	—	—	—	—	—	—	—
Chlorite	0.5	0.3	—	—	—	10.3	9.7	8.2	8.1	8.6	10.7	11.8	11.7	10.8	10.0	9.1	11.8	12.5	9.9	13.7	4.1	3.9	1.4	1.5	0.7	6.7	1.1
I/S	3.8	1.4	2.3	4.4	—	3.0	2.4	3.0	0.4	4.7	4.6	4.5	4.9	7.0	5.8	5.3	0.3	2.9	3.7	6.8	4.6	5.3	4.6	—	2.0	2.0	1.2
C/S	—	—	1.7	1.6	3.7	—	—	—	—	—	—	—	—	—	—	—	—	—	—	—	—	—	4.6	2.2	1.5	—	—
Gypsum	—	—	—	—	—	3.9	—	2.9	—	—	—	—	—	—	—	—	—	—	—	—	—	—	—	—	—	—	—
TOC	3.4	×	4.8	3.7	×	2.2	2.0	1.9	0.3	1.4	1.1	1.1	0.9	1.1	0.9	×	0.9	0.9	0.7	0.7	×	0.3	0.6	0.4	0.4	×	0.8

Note. I/S = illite/smectite mixed layer, C/S = chlorite/smectite mixed layer. "×" represents that the item was not tested.

formations. The Longmaxi shale gouge friction and stability were analyzed on the basis of the rate-and-state friction (RSF) experiments and theory. These experiments and analyses relate mineralogic composition to fault reactivation and instability and have important implications for seismic mechanisms in Longmaxi shales in particular and shales in general.

2. Material and Methods

2.1. Sample Preparation

A total of 27 shale samples were collected from across the stratigraphic section at Lijiawan Villiage (coordinates: 104°26′33.9″E, 28°07′55.4″N) (Figures 1 and 4). The surface weathered zone was removed to reveal unweathered Longmaxi formation shale that was recovered for the experiments (Figures 4b and 4c). The mineral compositions of the collected shale samples were analyzed by X-ray diffraction (XRD) at the Micro Structure Analytical Laboratory of Peking University, Beijing, China (instrument type: Rigaku D/max-rB). We first crushed and sieved the shale samples to obtain particle sizes <10 μm. The shale powders were then placed uniformly into a sealed channel and loaded into the X-ray diffractometer. Finally, the diffraction data were logged between 3° and 70° with a step interval of 0.02° and at 40 kV and 100 mA. Quantitative analysis of mineral content and calibration were determined following the methods described in Chung (1974) and Moore and Reynolds (1989). To ensure the accuracy of the data, the above procedures were performed by laboratory personnel.

The total organic carbon (TOC) contents were evaluated using a carbon sulfur analyzer (instrument type: LECO CS-230) following the procedures described in the standard "Determination of total organic carbon in sedimentary rock" (General Administration of Quality Supervision, Inspection and Quarantine of China, 2003) at the Laboratory Center at the PetroChina Hangzhou Research Institute of Geology. The shale samples were first ground to particle sizes <20 μm and saturated with hydrochloric acid solution to remove the inorganic carbon. Then the samples were dried and combusted in oxygen to convert the TOC into carbon dioxide (CO_2). Finally, the CO_2 content was evaluated by infrared detector and the TOC content calculated according to the standard (General Administration of Quality Supervision, Inspection and Quarantine of China, 2003). Results of mineral compositions (wt.%) and TOC contents (wt.%) for the collected shale samples are shown in Table 1 and Figure 5.

The mineral compositions of the sampled shales are variable (Figure 5). Following previous approaches (Behnsen & Faulkner, 2012; Kohli & Zoback, 2013; Moore & Lockner, 2004), we classified the mineral groups into tectosilicates, carbonates, and phyllosilicates and TOC. Illite and chlorite dominate the phyllosilicate content with minor quantities of kaolinite and smectite (Table 1). The tectosilicate contents decrease from the base of the section to the top, while carbonate contents increase (Figures 5 and S1). Combined phyllosilicate and TOC content is in the range of 20–40 wt.%, with the phyllosilicates and TOC contents of Samples 15# and 38# below 20 wt.%. We selected 10 shale samples with contrasting mineralogies (i.e., 10#, 14#, 15#, 19#, 28#, 29#, 32#, 33#, 35#, and 38#) as a likely representation of the spectrum of frictional properties of the Longmaxi formation shales. The 10 shale samples were crushed and sieved to a grain size <75 μm as representative of gouge. The particle size distribution of these 10 samples were determined by laser classifier (instrument type: Mastersizer 2000) as illustrated in Figure 6. $D(10)$, $D(50)$, and $D(90)$ magnitudes are presented in Table 2. The samples have median particle sizes $D(50)$ in the range 2–4 μm, except for Samples 14# ($D(50)$ = 19.8 μm) and 35# ($D(50)$ = 6.8 μm).

2.2. Testing Procedure

Shear experiments were conducted using an argon gas-confined triaxial shear apparatus (Figure 7) at the Institute of Geology, China Earthquake Administration, Beijing, China

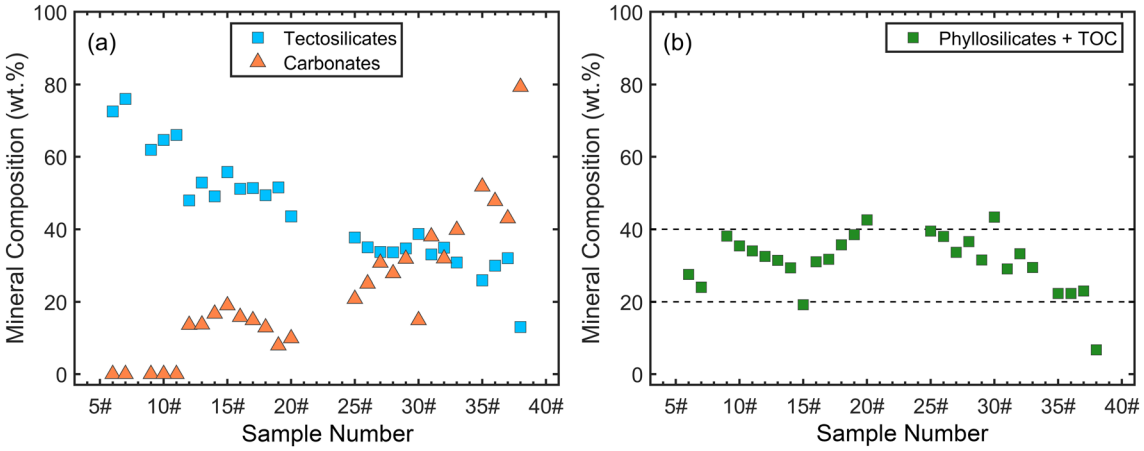

Figure 5. Mineral composition (wt.%) of the shale samples collected from the Longmaxi formation, representing (a) tectosilicates and carbonates, and (b) phyllosilicates and TOC. Tectosilicates comprise mainly quartz, albite, and orthoclase, and the carbonates mainly include calcite and dolomite.

(He et al., 2006; Zhang & He, 2016). The apparatus can apply a maximum confining pressure of 420 MPa and a maximum pore fluid pressure of 200 MPa at a maximum temperature of 600°C. The 1-mm thick shale powder was sandwiched between the 20-mm-diameter and 40-mm-height cylindrical stainless steel or gabbro driving blocks cut at 35° the loading axis. The assembled gouge thickness was controlled by a precise hollow cylindrical leveling jig. Sawcut surfaces of the gabbro driving blocks were uniformly ground using 200-mesh

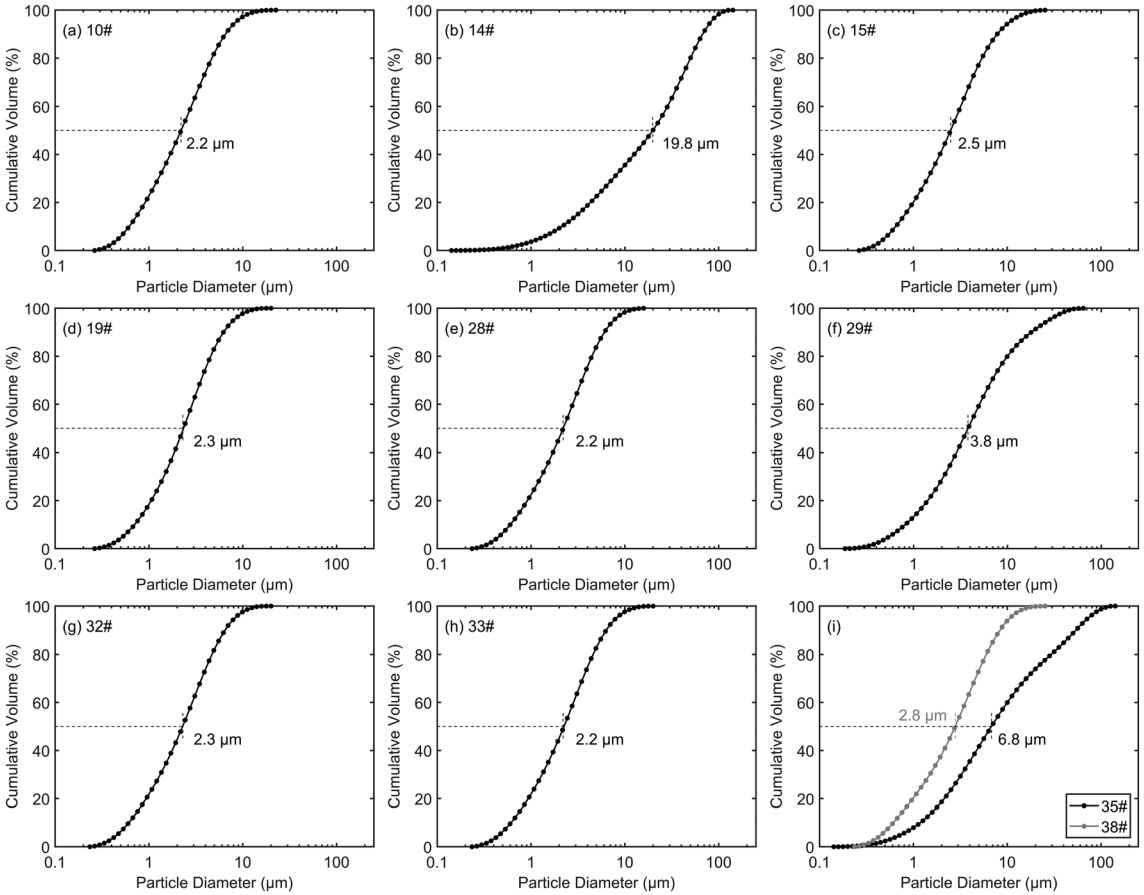

Figure 6. Particle size distributions of the 10 selected shale gouges, (a) 10#, (b) 14#, (c) 15#, (d) 19#, (e) 28#, (f) 29#, (g) 32#, (h) 33#, and (i) 35# and 38#.

Table 2
Particle Diameters Corresponding to D(10), D(50), and D(90) for the 10 Selected Shale Gouges (10#, 14#, 15#, 19#, 28#, 29#, 32#, 33#, 35#, and 38#)

Shale gouges	10#	14#	15#	19#	28#	29#	32#	33#	35#	38#
$D(10)$ (μm)	0.6	2.1	0.6	0.7	0.6	0.8	0.6	0.6	1.2	0.6
$D(50)$ (μm)	2.2	19.8	2.5	2.3	2.2	3.8	2.3	2.2	6.8	2.8
$D(90)$ (μm)	6.5	67.3	7.8	6.2	6.0	17.9	6.5	6.3	53.7	8.3

Note. $D(10)$ represents 10 vol.% particle size less than this diameter, similarly for $D(50)$ and $D(90)$.

silicon carbide, and the sawcut surfaces of the steel driving blocks were carved with 1-mm-width and 0.2-mm-depth grooves to prevent slippage at the sample-platen (steel or gabbro) contact. The upper steel or gabbro driving blocks were drilled with two mutually perpendicular boreholes (Figure 7) in order to maintain effective contact between the pore fluid and the gouge sample. Porous brass filters were inserted into the two boreholes to prevent the extrusion of gouge but maintain high permeability to the pore fluids. With the simulated gouges placed between the driving blocks, the gouge-filled steel or gabbro cylindrical driving blocks were subsequently inserted into a 0.35-mm thick annealed copper jacket (tube) with high-hardness corundum and tungsten carbide blocks on both sides. To prevent the convection of argon gas, the space between the copper tubing and furnace was loosely filled with high thermal and low electrical conductivity boron nitride. The O rings on both sides of the copper tubing were placed to prevent the argon gas from permeating into the gouge. The high-pressure seal in the upper piston contains any leakage of argon gas from the pressure vessel and enhances the sealing of the entire assembly. A thermocouple was inserted in the pore fluid inlet to monitor gouge temperature during the shear experiments.

The confining pressure was first applied by argon gas. The confining pressure and pore fluid pressure were maintained constant within ±0.5 and ±0.3 MPa, respectively, through two servo-controlled intensifiers. The temperature was raised by heating the furnace at a rate of 5°C/min and kept constant within ±2°C by an independent controller throughout the entire test. The recorded temperature reflects the temperature at the center of the gouge sample. The axial deformation was applied by an electrohydraulic servo control system and the axial displacement was recorded with an independent displacement sensor. The shear displacement was calculated from the axial displacement.

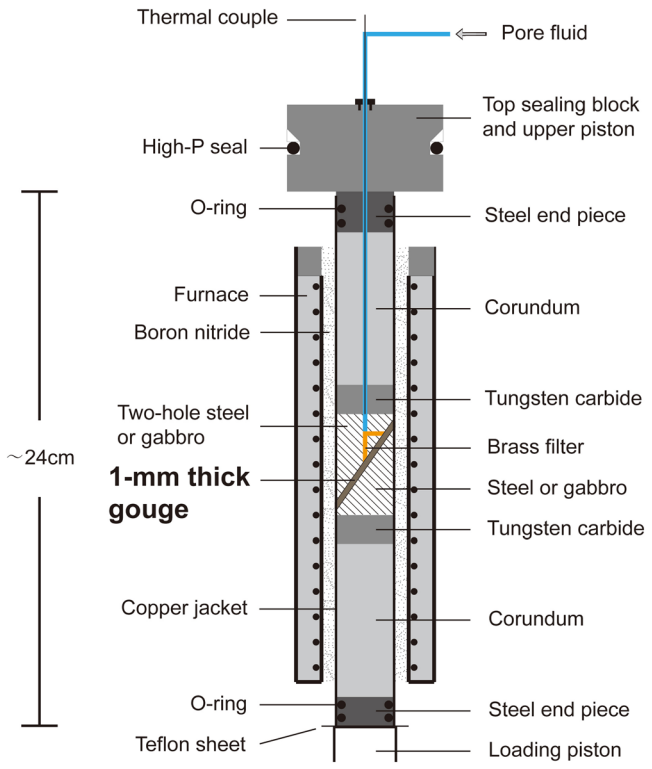

Figure 7. Triaxial shear assembly used for friction and stability experiments.

Ten experiments were conducted under a constant confining pressure (σ_c) of 60 MPa and a constant pore fluid pressure (P_f) of 30 MPa to characterize the frictional strength and stability of the 10 selected shale gouges (10#, 14#, 15#, 19#, 28#, 29#, 32#, 33#, 35#, and 38#) at a temperature (T) of 150°C. The confining pressure and pore fluid pressure are representative of the Longmaxi formation at the locations and depths for hydraulic fracturing in the Changning area (Chen et al., 2017). The temperature of 150°C represents a likely upper temperature limit of the Longmaxi formation in the Sichuan Basin and also is the critical temperature for the transformation of several clay minerals (den Hartog et al., 2012; Inoue & Utada, 1991; Jiang et al., 2016). Another three tests were performed under the same stress conditions but with temperatures varied from 30–300°C to explore the temperature dependence of Samples 15# and 38#. The temperature of 300°C is much higher than that likely for the Longmaxi shales at depths of 2–3 km. The experimental details are reported in Table 3. At the initiation of the shear experiments, all samples were stressed at a constant axial displacement rate of 1.0 μm/s. When the steady state friction was achieved, the axial displacement rates were stepped between 0.1 and 1.0 μm/s, equivalent to instantaneous displacement rates of 0.122 and 1.22 μm/s along the direction of shear. We failed to recover the gouge of Testing ID S38-150 initially completed on steel driving blocks for

Table 3
Matrix of Experimental Conditions

Testing ID	Shale gouges	σ_c (MPa)	P_f (MPa)	T (°C)	Driving blocks	l_{final} (mm)	Type of motion
S10-150	10#	60	30	150	Steel	3.35	vs
S14-150	14#	60	30	150	Steel	3.49	vs
S15-30	15#	60	30	30	Steel	3.60	vs
S15-150	15#	60	30	150	Steel	3.59	Mixed; vs, vw
S15-300	15#	60	30	300	Steel	3.58	Mixed; vw, ss
S19-150	19#	60	30	150	Steel	3.29	vs
S28-150	28#	60	30	150	Steel	3.24	vs
S29-150	29#	60	30	150	Steel	3.33	vs
S32-150	32#	60	30	150	Steel	3.22	vs
S33-150	33#	60	30	150	Steel	3.33	vs
S35-150	35#	60	30	150	Steel	3.51	vs
S38-90	38#	60	30	90	Steel	3.49	vs
S38-150	38#	60	30	150	Gabbro	3.83	Mixed; vs, vw

Note. σ_c = confining pressure, P_f = pore fluid pressure, T = temperature, l_{final} = final shear displacement, vs = velocity strengthening, vw = velocity weakening, ss = stick-slip.

microstructural analysis. The experiment was conducted again using gabbro driving blocks. Although changing the driving blocks could conceivably alter the system stiffness, this change would have negligible effect on the values of the coefficient of friction μ and $(a-b)$.

2.3. Data Analysis

During the shear experiments, the confining pressure, pore fluid pressure, temperature, piston load, and axial displacement were recorded at a sampling frequency of 10 Hz. To compensate for the effect of the variation in gouge contact/shear area and to remove the shear resistance of the annealed copper tubing, the raw logged data were corrected following the method described in He et al. (2006). The corrected data were subsequently processed to obtain values of normal stress (σ_n) and shear stress (τ). The coefficient of friction μ of the gouge is calculated as the ratio of the shear stress τ to effective normal stress σ_{neff} (ignoring the cohesion), expressed as

$$\mu = \frac{\tau}{\sigma_{neff}} = \frac{\tau}{(\sigma_n - P_f)} \tag{1}$$

Here, the shear velocity is the same as the displacement rate along the direction of shear.

The velocity dependence parameter $(a-b)$ was analyzed on the basis of RSF theory (Dieterich, 1978, 1979; Marone, 1998; Ruina, 1983). In the framework of RSF theory, the coefficient of friction μ is defined as

$$\mu = \mu_0 + a\ln\left(\frac{V}{V_0}\right) + b\ln\left(\frac{V_0\theta}{d_c}\right) \tag{2}$$

$$\frac{d\theta}{dt} = 1 - \frac{V\theta}{d_c} \tag{3}$$

where μ_0 is the coefficient of friction at the reference shear velocity V_0, μ is the coefficient of friction at the instantaneous shear velocity V, a and b are two constants that reflect the direct and evolutional effects of frictional resistance from the change in shear velocity, respectively (Figure S2a), d_c represents the critical slip distance required to reach a new steady state (Figure S2a), and θ is a state variable and denotes the contact age. The state variable θ remains constant and no longer evolves with time at steady state friction, and thus we have $d\theta/dt = 0$. The velocity dependence parameter $(a-b)$ can be calculated from Equations 2 and 3, expressed as

$$a - b = \frac{\Delta\mu_{ss}}{\Delta\, ln(V)} \tag{4}$$

where $\Delta\mu_{ss}$ is the difference in steady state coefficients of friction both before then after the velocity step.

Positive values of $(a - b)$ indicate velocity-strengthening behavior (Figure S2a). Fault gouges with positive $(a - b)$ promote inherently stable sliding and inhibit seismic fault rupture. Conversely, negative values of $(a - b)$ indicate velocity-weakening behavior where fault reactivation may be unstable and subject to seismic sliding when the critical stiffness criterion is also met (Figure S2b) (Gu et al., 1984; Leeman et al., 2016). Methods for calculating values of $(a - b)$ for different fault responses are illustrated in Figures S2a–S2c. When the gouge shows stick-slip behavior, the maximum coefficient of friction during stick-slip was adopted to calculate values of $(a - b)$ (Figure S2c) (e.g., Pluymakers et al., 2014). Moreover, the long-term strain strengthening or weakening trends were removed in calculating $(a - b)$ following the methods in Figure S2d.

2.4. Microstructural Methods

At conclusion of the shear experiments, the deformed gouge samples were first dried in an oven at 50°C for 2 days before being impregnated with epoxy resin in a vacuum chamber. When the adhesive was completely hardened, we cut thin sections from the gouge samples along the shear direction and the sample axis. Finally, all thin sections were polished and coated with carbon to allow microstructural imaging using scanning electron microscopy (SEM) (instrument type: Zeiss-sigma) and energy dispersive spectroscopy (EDS) (instrument type: Oxford-X-Max^{N}50).

3. Results

3.1. Frictional Strength and Stability

Following the procedure described in section 2.2, we conducted shear experiments on the 10 shale gouges at $\sigma_c = 60$ MPa, $P_f = 30$ MPa, and $T = 150$°C. The friction-displacement curves for the 10 shale gouges are presented in Figures 8a–8j. The near-linear increase in coefficient of friction μ in the first ~0.4 mm shear displacement in each experiment was eliminated in Figures 8a–8j. After ~1.0 mm shear displacement, each experiment exhibits a slight strain strengthening (e.g., shale gouge 15# in Figure 8c) or strain weakening (e.g., shale gouge 32# in Figure 8g) response. In particular, we observe a slip weakening trend for shale gouge 38# in Figure 8j. The coefficient of friction μ of shale gouge 38# is characterized by a distinct peak at ~1.0 mm shear displacement and then a decay to a steady state value with increasing shear displacement (Figure 8j). This phenomenon is possibly driven by shear-induced compaction and related alignment of carbonate particles (~80 wt.% carbonates in shale gouge 38#) (Saffer et al., 2001) in the initial stages of shear with similar results found in other carbonate-rich simulated gouges (Giorgetti et al., 2015). Another possible explanation is as a result of a transient increase in pore fluid pressure which may not be able to dissipate efficiently if the permeability of the gouge is low (Faulkner et al., 2018).

We evaluated the frictional strength μ at a shear velocity of 1.22 μm/s and ~3.0 mm shear displacement for all shear experiments (Figure 9a). The frictional stability $(a - b)$ was calculated based on the methods in section 2.3 with the results shown in Figure 9b and Table 4. The coefficient of friction μ of most shale gouges at $\sigma_c = 60$ MPa, $P_f = 30$ MPa, and $T = 150$°C are in the range ~0.5–0.6, except for shale gouges 15# ($\mu = 0.738$) and 38# ($\mu = 0.652$), consistent with previous laboratory results on simulated shale gouges or quartz-clay gouges with similar phyllosilicates contents (20–40 wt.%) (Kohli & Zoback, 2013; Moore & Lockner, 2011; Tembe et al., 2010) (Figure 9a and Table 4). A higher coefficient of friction in shale gouge 38# results from the higher content of carbonates (~80 wt.%) and lower phyllosilicate content (~6 wt.%) (Giorgetti et al., 2015) (Figure 9a and Table 1). Though shale gouge 15# has a relatively lower content of phyllosilicates (~19 wt.%), we postulate that the higher content of pyrite (~6 wt.%) in shale gouge 15#, relative to others (0–2 wt.%), may also contribute to its higher coefficient of friction (Figure 9a and Table 1). Most shale gouges (except for 15# and 38#) exhibit positive values of $(a - b)$ with $(a - b)$ spanning a range of ~0.005–0.010, indicating these gouges will promote fault stable sliding (Figure 9b and Table 4). To the contrary, both shale gouges 15# and 38# show apparent velocity-weakening behavior $(a - b < 0)$ and may promote unstable sliding whenever the critical stiffness criterion is met (Figure 9b). These friction data ($\mu = 0.5$–0.6, $a - b = 0.005$–0.010) of most of the gouges (except for 15# and 38#) (Figure 9) indicate that the frictional properties are mainly controlled by the phyllosilicate content and are little affected by the relative change in proportions of tectosilicates or carbonates. Negative $(a - b)$ values paired with higher coefficients of friction μ (Figure 9) are in accordance with the relationship of fault frictional strength and stability summarized by Ikari et al. (2011).

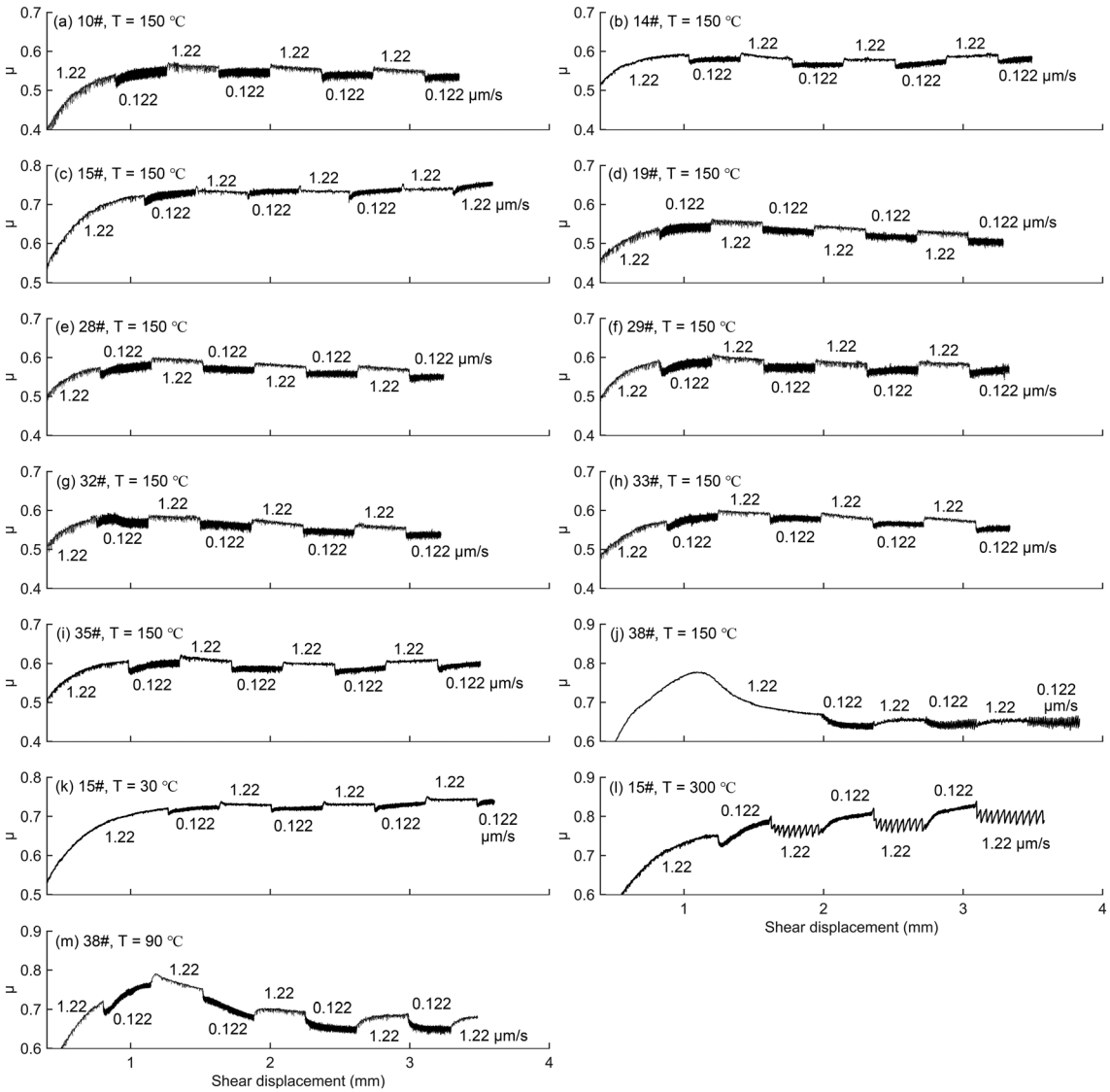

Figure 8. Coefficient of friction (μ) versus shear displacement for shale gouges: (a) 10#, (b) 14#, (c) 15#, (d) 19#, (e) 28#, (f) 29 #, (g) 32#, (h) 33#, (i) 35#, and (j) 38# at $\sigma_c = 60$ MPa, $P_f = 30$ MPa, and $T = 150$°C; (k and l) 15# at $\sigma_c = 60$ MPa, $P_f = 30$ MPa, and $T = 30$ and 300°C; and (m) 38# at $\sigma_c = 60$ MPa, $P_f = 30$ MPa, and $T = 90$°C.

3.2. Temperature Effects on Gouge Friction

To examine the temperature dependence of friction and stability, we further varied the testing temperature of shale gouges 15# and 38#. The friction-displacement curves for shale gouges 15# and 38# at $\sigma_c = 60$ MPa, $P_f = 30$ MPa, and temperatures in the range 30–300°C are shown in Figures 8c and 8j–8m. For shale gouge 15# at $T = 300$°C (Figure 8l), the friction-displacement curves show apparent stick-slip at a shear velocity of 1.22 μm/s with this stick-slip indicative of seismic response (Brace & Byerlee, 1966).

Trends in coefficient of friction μ and frictional stability ($a - b$) with applied temperature for shale gouges 15# and 38# are illustrated in Figure 10. The coefficient of friction of shale gouge 15# is independent of temperature ($\mu = \sim 0.74$) in the range 30–150°C but increases to $\mu = \sim 0.8$ at $T = 300$°C (Figure 10a and Table 4). This sample exhibits a transition from velocity strengthening at $T = 30$°C ($a - b = \sim 0.0035$), to weak velocity weakening at $T = 150$°C ($a - b = -0.0003$ to -0.0011), and to stronger velocity weakening and stick-slip at $T = 300$°C ($a - b = -0.0045$ to -0.0055) (Figures 8k, 8l and 10b, Table 4). For shale gouge 38#, the coefficient of friction at $T = 150$°C ($\mu = \sim 0.65$) is slightly lower than that at $T = 90$°C ($\mu = \sim 0.68$), with a change from

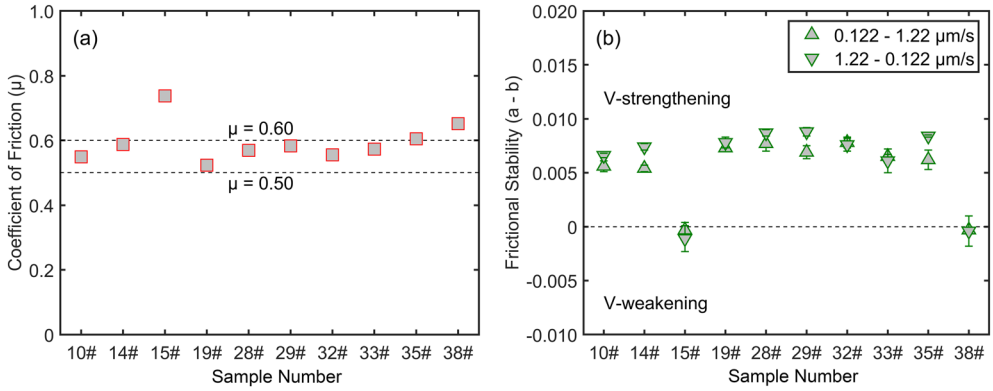

Figure 9. (a) Coefficient of friction μ of the shale gouges at $\sigma_c = 60$ MPa, $P_f = 30$ MPa, and $T = 150$°C. The coefficient of friction μ in each test is evaluated at a shear displacement of ~3.0 mm and at a shear velocity of 1.22 μm/s. (b) The frictional stability $(a - b)$ of the shale gouges at $\sigma_c = 60$ MPa, $P_f = 30$ MPa, and $T = 150$°C. Error bar indicates the standard deviation from the same velocity steps in each shear experiment.

strong velocity strengthening at $T = 90$°C $(a - b = \sim 0.0150)$ to weak/neutral velocity weakening at $T = 150$°C $(a - b = -0.0003$ to $-0.0004)$ (Figure 10b and Table 4).

3.3. Microstructural Characterization

We focus on microstructural characteristics of the shale gouges at $T = 150$°C. The microstructures along the shear direction for four sheared samples (10#, 15#, 29#, and 38#) were compared (Figures 11 and 12) using SEM in backscattering electron mode. Shale gouge 10# shows no apparent shear with fractures caused by unloading the sample. Granular flow of gouge particles with elongated minerals is observed in shale gouge 29#. These two shale gouges (10# and 29#) both show velocity-strengthening responses at the macro scale. Conversely, shale gouges 15# and 38#, exhibiting velocity-weakening behavior, show apparent R_1 shears (Figures 11c and 11d) and significantly local grain crushing along the R_1 shears (Figures 12c and 12d) (Logan et al., 1992). This is in accordance with previous laboratory results that local shear regions can be found in deformed gouges that undergo velocity weakening (He et al., 2016; Sawai et al., 2016).

Table 4
Coefficient of Friction μ and Calculated Velocity Dependence $(a - b)$ in Each Experiment

Testing ID	μ	$(a - b)$ in upward velocity step	$(a - b)$ in downward velocity step
S10-150	0.549	0.0056 ± 0.0005	0.0066 ± 0.0002
S14-150	0.587	0.0054 ± 0.0003	0.0074 ± 0.0003
S15-30	0.743	0.0037 ± 0.0003	0.0035 ± 0.0004
S15-150	0.738	−0.0003 ± 0.0007	−0.0011 ± 0.0012
S15-300	0.801	−0.0055 ± 0.0012	−0.0045 ± 0.0005
S19-150	0.523	0.0073	0.0078 ± 0.0005
S28-150	0.569	0.0077 ± 0.0007	0.0087 ± 0.0003
S29-150	0.583	0.0069 ± 0.0006	0.0088 ± 0.0004
S32-150	0.555	0.0078 ± 0.0005	0.0076 ± 0.0006
S33-150	0.573	0.0065 ± 0.0002	0.0061 ± 0.0011
S35-150	0.605	0.0062 ± 0.0009	0.0084 ± 0.0001
S38-90	0.684	0.0147 ± 0.0008	0.0153
S38-150	0.652	−0.0003	−0.0004 ± 0.0014

Note. Upward velocity step = velocity step from 0.122 to 1.22 μm/s, downward velocity step = velocity step from 1.22 to 0.122 μm/s.

4. Discussion

4.1. Depositional Controls on Mineralogical Variation

The Longmaxi formation shales show a strong variation in mineral composition (Figure 5), characterized by a decreasing proportion of tectosilicates and increasing proportion of carbonates with a rise across the stratigraphic section. The mineralogic variation across the Longmaxi formation is mainly affected by the depositional setting (Hao et al., 2013; Ju et al., 2014).

The Lower Silurian Longmaxi formation shales are marine shales widely distributed in the Sichuan Basin and adjacent areas of southwest China (Liang et al., 2014; Wang et al., 2015; Xu et al., 2019). The south China experienced a quasi-symmetrical intracontinental shortening in the Silurian period and this led to crustal thickening and changes in sea level (Charvet, 2013). The changes in sea level and depositional environment are reflected in the mineralogy of the Longmaxi formation shales. We compared the variations in four different marker minerals, that is, quartz, feldspar, calcite, and TOC in the $S_1l_{1\text{-}1}$ and $S_1l_{1\text{-}2}$ subsections and S_1l_2 section of the Longmaxi formation in Figure 13. Shales in the $S_1l_{1\text{-}1}$ subsection show the highest quartz content (generally >35 wt.%) with the quartz content

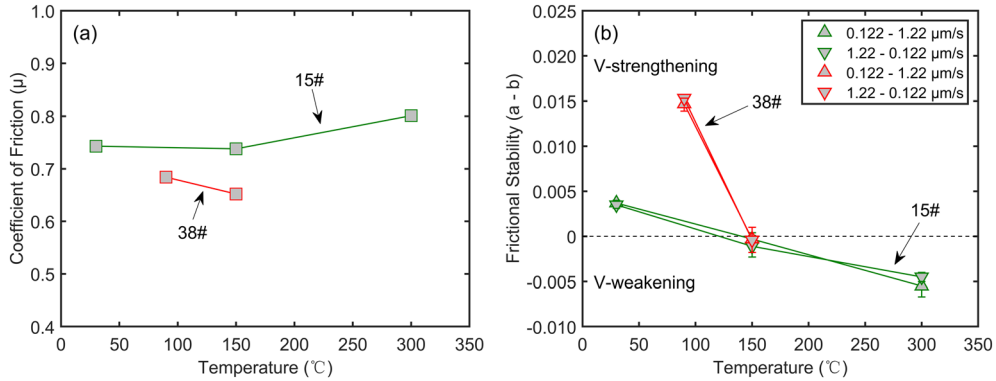

Figure 10. (a) Coefficient of friction μ and (b) frictional stability ($a - b$) for shale gouges 15# and 38# at $\sigma_c = 60$ MPa, $P_f = 30$ MPa, and for different temperatures. The coefficient of friction μ in each test is evaluated at a shear displacement of ~3.0 mm and a shear velocity of 1.22 μm/s. The error bars in (b) represent the standard deviation from the same velocity steps in each shear experiment.

decreasing in shales of the $S_1l_{1\text{-}2}$ (20–40 wt.%) and S_1l_2 sections (~20 wt.%) (Figure 13a). A higher content of feldspar is present (10–20 wt.%) in shales of the $S_1l_{1\text{-}1}$ subsection and the lower part of the $S_1l_{1\text{-}2}$ subsection, with a lower content (10 wt.%) in the upper part of the $S_1l_{1\text{-}2}$ subsection and S_1l_2 section (Figure 13b). The calcite content steadily increases from <10 wt.% in shales of the $S_1l_{1\text{-}1}$ subsection to 10–30 wt.% in shales of the $S_1l_{1\text{-}2}$ subsection and 30–80 wt.% in shales of the S_1l_2 section (Figure 13c). Finally, the TOC content gradually decreases from >2 wt.% in shales of the $S_1l_{1\text{-}1}$ subsection to 1–2 wt.% in shales of the $S_1l_{1\text{-}2}$ subsection and <1 wt.% in the S_1l_2 section (Figure 13d). These data demonstrate that siliceous minerals (e.g., quartz and feldspar) are abundant and carbonate minerals are depleted in shales of the $S_1l_{1\text{-}1}$ subsection, and the converse in shales of the S_1l_2 section. Based on the nomenclature for the depositional settings of the Paleozic marine shales in south China (e.g., Xu et al., 2019), we postulate that the $S_1l_{1\text{-}1}$ and S_1l_2 shales were deposited in intrashelf and shallow-shelf environments, respectively. The depositional setting of the $S_1l_{1\text{-}2}$ shales was in a transitional area between this intrashelf and the shallow shelf. The intrashelf regions are enriched in siliceous minerals (e.g., quartz and feldspar) and TOC derived from the presence of ocean creatures (Hawkins et al., 2017). A drop in sea level in the shallow shelf reduced the

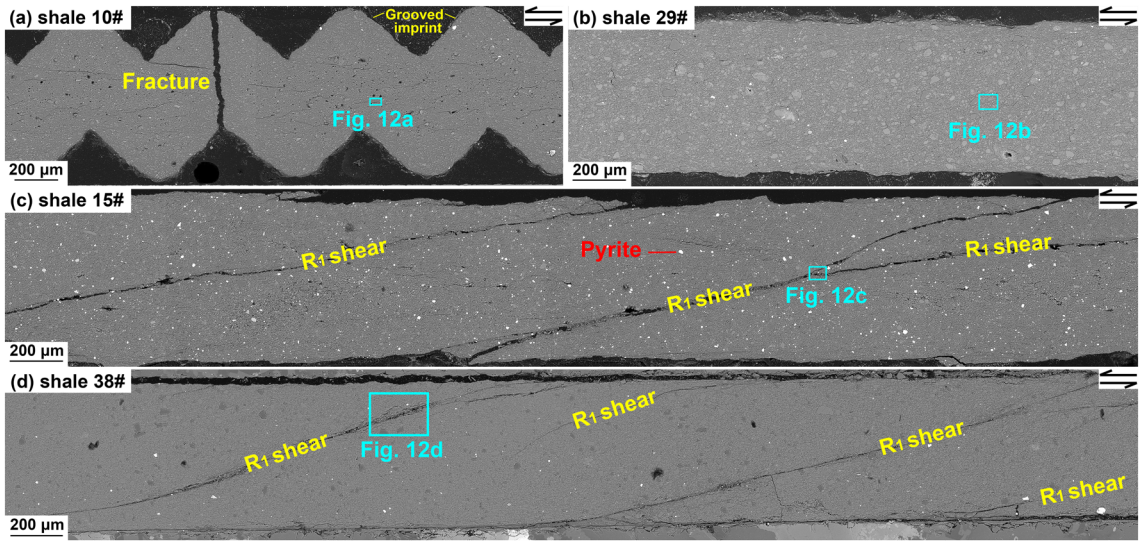

Figure 11. Microstructures of the deformed gouges (backscattered images) at $\sigma_c = 60$ MPa, $P_f = 30$ MPa, and $T = 150$°C, for shale gouges (a) 10#, (b) 29#, (c) 15#, and (d) 38#. Shear localization features were described by referencing the methods of Logan et al. (1992). For (a) and (b), the gouges exhibit velocity-strengthening behavior with velocity-weakening responses observed in (c) and (d).

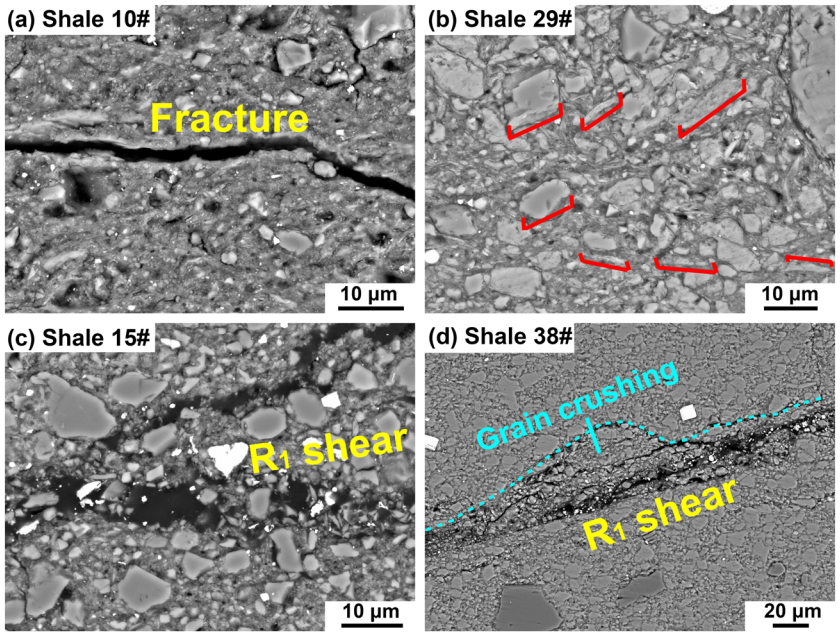

Figure 12. Microstructures of deformed shale gouges (a) 10#, (b) 29#, (c) 15#, and (d) 38# at $\sigma_c = 60$ MPa, $P_f = 30$ MPa, and $T = 150$°C. The areas in (a)–(d) are marked in Figure 11. The fracture in (a) was caused by unloading the sample after the experiment. The red lines in (b) indicate the minerals elongated and deformed during shear, and the cyan dashed lines show the area of strong grain crushing.

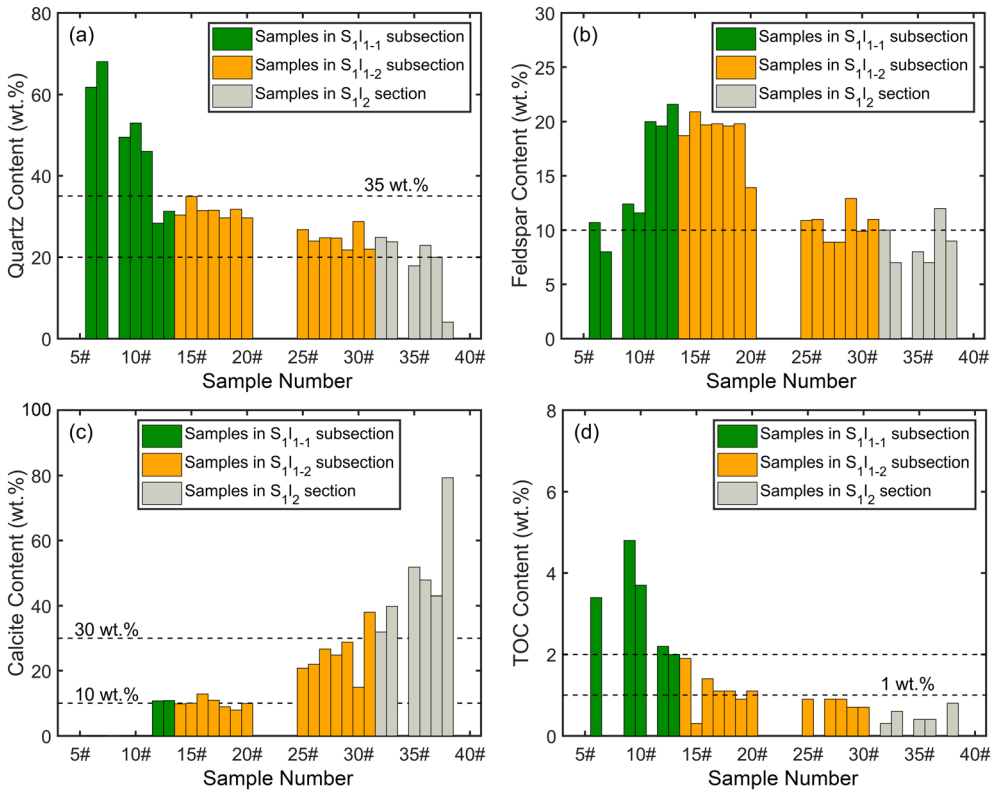

Figure 13. Single mineral content (wt.%) of the collected shale samples in each section or subsection of the Longmaxi formation, (a) quartz, (b) feldspars (mainly including albite and orthoclase), (c) calcite, and (d) TOC.

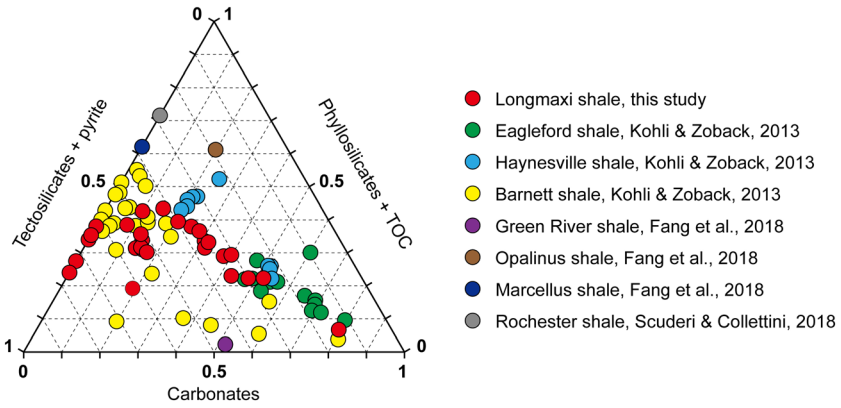

Figure 14. Mineral compositions of different shale samples in the ternary space of wt.% tectosilicates and pyrite, phyllosilicates and TOC, and carbonates. Compilation from this and previous studies (Fang et al., 2018; Kohli & Zoback, 2013; Scuderi & Collettini, 2018).

number of ocean creatures and thus reduced the contents of siliceous minerals and TOC (Figure 13). In addition, large amounts of carbonate minerals can be deposited on the shallow shelf (Mount, 1984; Rankey, 2004), and this is in accordance with the observed higher calcite content in the S_1l_2 section.

4.2. Dependence of Shale Gouge Friction on Mineralogy

The Longmaxi formation shales show a significant variation in mineral composition reflecting different depositional settings. This mineralogical variation can also influence the frictional strength and stability of the gouges. We compare the mineral compositions of Longmaxi formation shales with other reported shales in Figure 14 (viz. Eagleford, Haynesville and Barnett shales (Texas and Louisiana, USA) (Kohli & Zoback, 2013), Green River shale (Colorado, USA), Opalinus shale (Switzerland), Marcellus shale (Pennsylvania, USA) (Fang et al., 2018), and Rochester shale (West Virginia, USA) (Scuderi & Collettini, 2018). The shale samples are classified as mixtures of three groups of minerals, that is, tectosilicates and pyrite, phyllosilicates and TOC, and carbonates, ignoring other low-content minerals (e.g., gypsum). These shales are highly variable in composition and cover the majority of the ternary space of Figure 14. We further compare the measured frictional strength μ and stability $(a - b)$ for different fault gouges with varied proportions of this ternary group of minerals, both from this study and from previous studies (Boulton et al., 2012; Fang et al., 2017; Giorgetti et al., 2015; Kohli & Zoback, 2013; Moore & Lockner, 2011; Zhang et al., 2019) in Figure 15. Compared with phyllosilicate and TOC-rich gouges (top vertex of the ternary plot), the tectosilicate and pyrite-rich (basal left vertex) and carbonate-rich (basal right vertex) gouges generally exhibit higher frictional strength μ and lower frictional stability $(a - b)$ manifested as velocity-weakening behavior. This indicates that tectosilicates + pyrite-rich and carbonate-rich gouge-filled faults have a greater potential for seismic slip. Thus, the variation in proportions of tectosilicates + pyrite, phyllosilicates + TOC, and carbonates in shales potentially exert a control on the style of fault reactivation—defining a potential spectrum of behaviors from aseismic to seismic.

The best quality shale reservoirs are typically located in both TOC-rich and brittle mineral (quartz)-rich shales (Loucks & Ruppel, 2007; Xu et al., 2019). High TOC content is a prerequisite for high intrinsic gas content and high brittleness favors the production of long and pervasive fractures during hydraulic fracturing that potentially enhance reservoir permeability (Zhang et al., 2017). However, an increase in the proportion of brittle minerals may have an adverse effect on the stability of preexisting faults and promote seismic response during fault reactivation (Figure 15).

4.3. Anatomy of Current Seismicity

In the Changning and Weiyuan areas, the target reservoirs for hydraulic fracturing are mainly located at Silurian Longmaxi shales at a depth of ~2–3 km (Lei et al., 2017). Current swarms of earthquakes in this depth range are strongly correlated with hydraulic fracturing. The average temperature gradient in these areas is ~25–35°C/km (Xi et al., 2018) resulting in temperatures at 2–3 km in the range of 50–105°C.

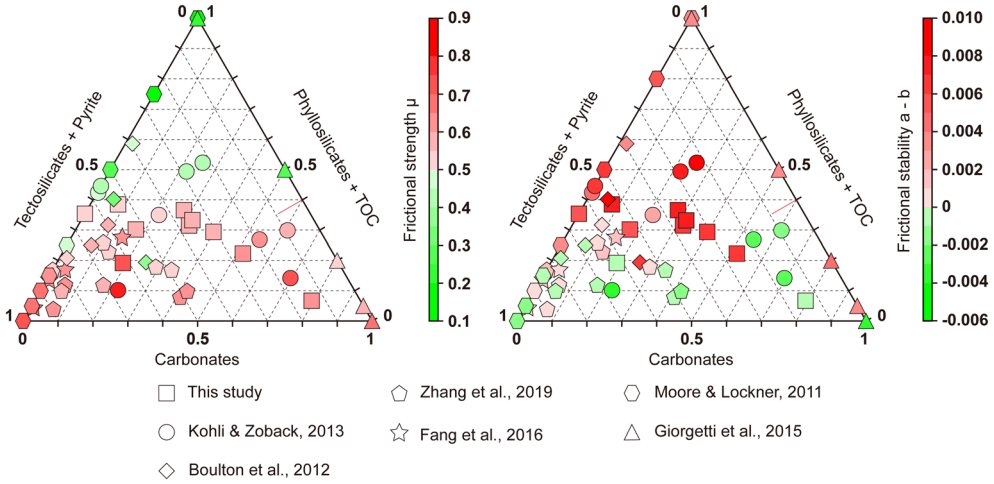

Figure 15. (left) Frictional strength μ and (right) frictional stability $(a - b)$ for gouges with different proportions of tectosilicates and pyrite, phyllosilicates and TOC, and carbonates both from this study and previous laboratory results (Boulton et al., 2012; Fang et al., 2016; Giorgetti et al., 2015; Kohli & Zoback, 2013; Moore & Lockner, 2011; Zhang et al., 2019). The red symbols in the left panel indicate $\mu > 0.5$, and the green symbols represent $\mu < 0.5$. The red and green symbols in the right panel denote either velocity-strengthening $(a - b > 0)$ or velocity-weakening $(a - b < 0)$ behaviors, respectively. The symbols closer to the top, left basal, and right basal vertices indicate phyllosilicate and TOC-rich, tectosilicate and pyrite-rich, and carbonate-rich gouges, respectively. All data are listed in Table S1 in the supporting information.

Lithostatic stress is in the range 50–75 MPa (with rock density of 2,500 kg/m^3) with fluid pressures (hydrostatic pressures) of 20 to 30 MPa. However, on the basis of our shear experiments (Figure 9) most of the shale gouges at 50–105°C, $\sigma_c = 60$ MPa and $P_f = 30$ MPa promote velocity-strengthening behavior —thus, the preexisting faults should be inherently stable and aseismic. This clearly contradicts the field observation of clusters of earthquakes (Figure 2). Compared with previous studies that explored the mineralogy of Longmaxi shales (e.g., Liang et al., 2014; Xu et al., 2019) the phyllosilicate + TOC-poor (<20 wt.%) shales account for only a small proportion of the stratigraphic section with the majority of shales showing higher contents of phyllosilicate + TOC. Therefore, most preexisting faults accessed by the injected hydraulic fracturing fluids should deform stably. This implies that many of the observed earthquakes are not directly related to fluid injection increasing local pore pressures and reducing effective normal stress and strength and thereby promoting aseismic slip in these formations. Thus, an alternative mechanism of generating seismicity must be invoked. The third hypothesis for induced earthquakes that we previously introduced (Figure 3) is that of indirect triggering by aseismic slip caused by the fluid injection. Given the stable behavior of the Longmaxi shales, this model seems intuitively to be the most likely explanation for the generation of induced earthquakes in the region and is further explored in the following.

4.4. Seismic Response Induced by Aseismic Slip

An important remaining question is how the observed seismic response may be induced by what is presumed to be aseismic slip on faults within the high-phyllosilicate + TOC Longmaxi section. We provide several possible explanations here with discussion as follows.

First, based on the observations of the varied mineral compositions in shale reservoir, we postulate that aseismic slip on subsurface faults may reactivate adjacent unstable faults and trigger seismicity. From the shear experiments, several rock layers within the Longmaxi formation exhibit higher frictional strength but a velocity-weakening trend (Figure 9 and Table 4). Gouge-filled faults within these layers have the potential for unstable slip provided the patch size is sufficient to meet the critical stiffness criterion. The experimental data presented in this study indicate that the frictional properties of Longmaxi shale are heterogeneous and potentially unstable layers exist in the formation. One potential mechanism (Figure 16) is where fluid injection drives slip on aseismic faults with stress transfer onto adjacent

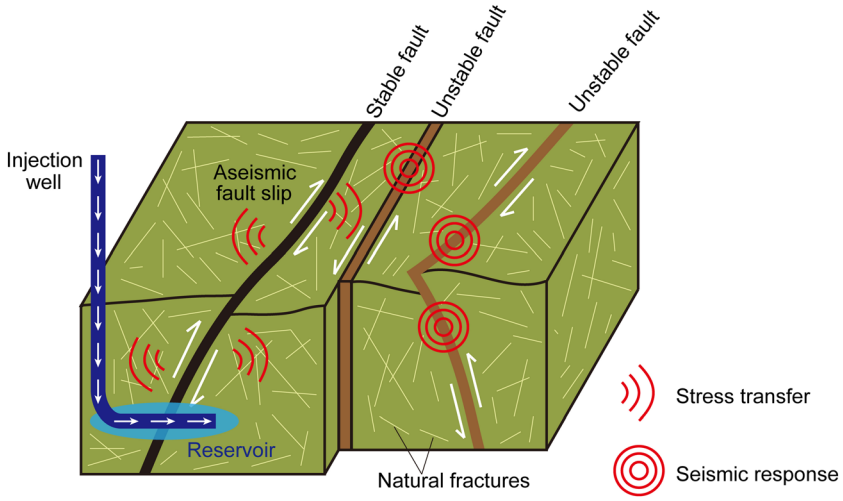

Figure 16. Schematic of stress transfer from injection-local aseismic slip generating distal seismic slip.

unstable and critically stressed faults (Wang et al., 2003; Ziv & Rubin, 2000). The Coulomb failure stress (ΔCFS) may be used to define the propensity for failure (King et al., 1994) as

$$\Delta \mathrm{C}FS = \Delta\tau - \mu_s \cdot \Delta\sigma_{neff} \tag{5}$$

where $\Delta\tau$ and $\Delta\sigma_{neff}$ are the change in shear stress and effective normal stress on the fault plane and μ_s is the static coefficient of friction. Previous observations suggest that even very small changes in Coulomb failure stress (ΔCFS), of the order of $\Delta CFS = 0.01$ MPa (Stein, 1999) may reactivate faults that are critically stressed and trigger seismicity. This suggests that even minor stress transfer resulting from injection-local aseismic slip may trigger distal seismic slip.

Second, we infer that aseismic slip is induced by the hydraulic fracturing within the reservoir, that is, the Longmaxi formation. We speculate that this would load adjacent faults and could trigger earthquakes either in the formation above or below. This extrapolation is based on the model of Eyre et al. (2019) where distant fault ruptures could be induced by aseismic fault slip at reservoir depth. The adjacent Lower Silurian Shiniulan and Upper Ordovician Linxiang formations (Figure S1, Xu et al., 2019) both contain thick carbonate sequences (limestone) and carbonates are potentially unstable at fracturing depths of 2–3 km (Chen et al., 2015). This implies that the pore pressure-driven aseismic fault slip within the Longmaxi formation could induce earthquakes in the adjacent Shiniulan or Linxiang formations or other adjacent formations containing earthquake-prone rock types. The magnitudes of largest events are close to M_L 4.0, corresponding to a slip area of the order of ~1 km^2. The thickness of the Shiniulan formation is >600 m in the Sichuan Basin; thus, this formation is sufficiently thick to contain and thereby sustain such a rupture (Eyre et al., 2019; Xu et al., 2019). Although the earthquakes detected on the surface-mounted regional network appear to locate at depths between 2 and 3 km, corresponding to the Longmaxi formation, this formation only has a thickness of tens to hundreds of meters. Hence, it is plausible that many of the events are not entirely contained within the Longmaxi formation itself and transect adjacent formations. This is furthermore likely since the depth constraints on hypocenters from the surface-mounted regional monitoring network are known to be poorly constrained (Eisner et al., 2009).

Third, for shale gouges with likely low permeabilities, the effect of pore pressure transients within the gouges can also exert a strong influence on their frictional behavior (Faulkner et al., 2018). If the undrained pore fluid pressure within shale gouge is positive and nonequilibrated, it may promote frictional behavior transiting from velocity strengthening to velocity weakening. This is especially important for Longmaxi shale gouges as Longmaxi shale exhibits low porosity and extremely low permeability (Zhou et al., 2019).

Either of these three possible explanations could explain the occurrence of induced earthquakes in the Changning and Weiyuan areas and earthquakes may draw on a combination of the above mechanisms.

4.5. Implications for Shale Gas Exploitation

Seismicity accompanying hydraulic fracturing is closely related to the reactivation of preexisting faults. Our experimental results suggest a predominantly aseismic response of the Longmaxi formation to fault slip. However, seismicity may still occur when pore pressure-driven aseismic fault slip induces seismogenic rupture on adjacent or distant faults which exhibit velocity-weakening behavior. Thus, the absence, or low abundance, of velocity-weakening materials is not a guarantor of avoiding seismicity. The magnitude of the seismic events is also related to reservoir depth and fault size. The observed frictional trends with temperature infer that temperature is an important factor controlling fault stability and that fault instability will therefore be more pronounced at greater depths (Figure 10). However, the temperature of the Longmaxi formation shales at current fracturing depths (2–3 km) would be limited to below 150°C. The temperature effect would be more pronounced during future hydraulic fracturing at a much greater depth (e.g., 6–7 km) (Xu et al., 2019). For a circular fault (Brune, 1970; Vouillamoz et al., 2016), the earthquake magnitude (Zoback & Gorelick, 2012) scales with the cube of fault length—implied as the tributary volume from which the strain energy is recovered. This highlights the importance of identifying preexisting large-scale faults during shale gas exploration—not only in the area of injection but also remote from this area, where stress transfer may trigger failure. Identification of subsurface faults and assessing slip potential are beneficial in both minimizing the seismic hazard and associated risk during hydraulic fracturing and in enhancing productivity.

5. Conclusions

We report a systematic study of Longmaxi formation shale reservoir rocks from the Sichuan Basin of southwest China to investigate the frictional and stability properties of shale gouges. These are completed under conditions typified by the reservoir depth and applied to explain mechanisms controlling the clusters of earthquakes observed during hydraulic fracturing. The following conclusions are drawn:

1. The depositional settings of the Longmaxi formation shales underwent a marine transition from intrashelf to shallow shelf with this resulting in a broad variation in mineral composition. Intrashelf ($S_1l_{1\text{-}1}$ subsection) shales show higher contents of tectosilicates and TOC but less carbonates, with the opposite trend for the shallow-shelf (S_1l_2 section) shales.
2. The frictional and stability properties of these Longmaxi shale gouges are mainly controlled by the proportion of phyllosilicates + TOC. The frictional strengths μ of the majority shale gouges (containing ~20–40 wt.% phyllosilicates + TOC) are in the range of 0.5–0.6, and all exhibit velocity-strengthening behavior ($a - b > 0$). Two shale gouges with less phyllosilicates + TOC (<20 wt.%) show higher frictional strength ($\mu > 0.6$) but velocity-weakening behavior ($a - b < 0$) and may promote potentially unstable slip. These unstable shales account for ~5 wt.% of the stratigraphic section.
3. Temperature exerts a significant control on the stability of the shale gouge. In the temperature range (30–300°C), instability is more pronounced at higher temperatures.
4. The heterogeneous frictional properties of the Longmaxi shale gouges reflect that both stable and unstable faults are present in the targeted reservoir rocks. Considering the likely small proportion of unstable preexisting faults, we infer that some earthquakes are not directly triggered as a result of fluid injection. Instead, we postulate that increased pore fluid pressures due to fluid injection drive the deformation of aseismic faults. The aseismic fault slip could in turn reactivate adjacent unstable faults in the same formation and potentially also distant seismogenic faults in adjacent formations, triggering the observed seismicity. For the low-permeability Longmaxi shale gouges, the pore pressure transients within the gouge could also significantly affect the frictional behavior of the gouge. Since seismicity may be triggered by both stable and unstable fault slip, it is necessary to identify the presence and characteristics of large-scale faults during shale gas exploration, prior to extraction and to analyze the potential for fault slip and to minimize the seismic hazard.

Data Availability Statement

The earthquake data in this paper were recovered online (from www.data.earthquake.cn). The friction data in this work can be found online (at https://doi.org/10.5061/dryad.37pvmcvg9).

Acknowledgments

This research is funded by the key innovation team program of innovation talents promotion plan by MOST of China (2016RA4059), the National Natural Science Foundation of China (41672268 and 41941018), and the Fundamental Research Funds for the Central Universities (22120200081). We appreciate the assistance of Changrong He, Jianye Chen, and Xi Ma in conducting the experiments and acknowledge useful discussions with Yi Fang. We thank the Editor and two reviewers whose comments significantly improved the manuscript.

References

Bao, X., & Eaton, D. W. (2016). Fault activation by hydraulic fracturing in western Canada. *Science*, *354*(6318), 1406–1409. https://doi.org/10.1126/science.aag2583

Behnsen, J., & Faulkner, D. R. (2012). The effect of mineralogy and effective normal stress on frictional strength of sheet silicates. *Journal of Structural Geology*, *42*, 49–61. https://doi.org/10.1016/j.jsg.2012.06.015

Bhattacharya, P., & Viesca, R. C. (2019). Fluid-induced aseismic fault slip outpaces pore-fluid migration. *Science*, *364*(6439), 464–468. https://doi.org/10.1126/science.aaw7354

Boulton, C., Carpenter, B. M., Toy, V., & Marone, C. (2012). Physical properties of surface outcrop cataclastic fault rocks, Alpine Fault, New Zealand. *Geochemistry, Geophysics, Geosystems*, *13*, Q01018. https://doi.org/10.1029/2011GC003872

Brace, W. F., & Byerlee, J. D. (1966). Stick-slip as a mechanism for earthquakes. *Science*, *153*(3739), 990–992. https://doi.org/10.1126/science.153.3739.990

Brune, J. N. (1970). Tectonic stress and the spectra of seismic shear waves from earthquakes. *Journal of Geophysical Research*, *75*(26), 4997–5009. https://doi.org/10.1029/JB075i026p04997

Cappa, F., Scuderi, M. M., Collettini, C., Guglielmi, Y., & Avouac, J. P. (2019). Stabilization of fault slip by fluid injection in the laboratory and in situ. *Science Advances*, *5*, eaau4065. https://doi.org/10.1126/sciadv.aau4065

Charvet, J. (2013). The Neoproterozoic-Early Paleozoic tectonic evolution of the South China Block: An overview. *Journal of Asian Earth Sciences*, *74*, 198–209. https://doi.org/10.1016/j.jseaes.2013.02.015

Chen, J., Verberne, B. A., & Spiers, C. J. (2015). Interseismic re-strengthening and stabilization of carbonate faults by "non-Dieterich" healing under hydrothermal conditions. *Earth and Planetary Science Letters*, *423*, 1–12. https://doi.org/10.1016/j.epsl.2015.03.044

Chen, S., Zhu, Y., Qin, Y., Wang, H., Liu, H., & Fang, J. (2014). Reservoir evaluation of the Lower Silurian Longmaxi formation shale gas in the southern Sichuan Basin of China. *Marine and Petroleum Geology*, *57*, 619–630. https://doi.org/10.1016/j.marpetgeo.2014.07.008

Chen, Z., Shi, L., & Xiang, D. (2017). Mechanism of casing deformation in the Changning–Weiyuan national shale gas demonstration area and countermeasures. *Natural Gas Industry B*, *4*(1), 1–6. https://doi.org/10.1016/j.ngib.2017.07.001

Chung, F. H. (1974). Quantitative interpretation of X-ray diffraction patterns of mixtures. I. Matrix-flushing method for quantitative multicomponent analysis. *Journal of Applied Crystallography*, *7*(6), 519–525. https://doi.org/10.1107/S0021889874010375

den Hartog, S. A. M., Niemeijer, A. R., & Spiers, C. J. (2012). New constraints on megathrust slip stability under subduction zone *P–T* conditions. *Earth and Planetary Science Letters*, *353-354*, 240–252. https://doi.org/10.1016/j.epsl.2012.08.022

Deng, K., Liu, Y., & Harrington, R. M. (2016). Poroelastic stress triggering of the December 2013 crooked Lake, Alberta, induced seismicity sequence. *Geophysical Research Letters*, *43*, 8482–8491. https://doi.org/10.1002/2016GL070421

Dieterich, J. H. (1978). Time-dependent friction and the mechanics of stick-slip. *Pure and Applied Geophysics*, *116*(4–5), 790–806. https://doi.org/10.1007/BF00876539

Dieterich, J. H. (1979). Modeling of rock friction: 1. Experimental results and constitutive equations. *Journal of Geophysical Research*, *84*(B5), 2161–2168. https://doi.org/10.1029/JB084iB05p02161

Eisner, L., Duncan, P. M., Heigl, W. M., & Keller, W. R. (2009). Uncertainties in passive seismic monitoring. *The Leading Edge*, *28*(6), 648–655. https://doi.org/10.1190/1.3148403

Ellsworth, W. L., Townend, J., Zoback, M. D., Evans, K. F., Zappone, A., Kraft, T., et al. (2013). Injection-induced earthquakes. *Science*, *341*, 1225942. https://doi.org/10.1126/science.1225942

Elsworth, D., Spiers, C. J., & Niemeijer, A. R. (2016). Understanding induced seismicity. *Science*, *354*(6318), 1380–1381. https://doi.org/10.1126/science.aal2584

Eyre, T. S., Eaton, D. W., Garagash, D. I., Zecevic, M., Venieri, M., Weir, R., & Lawton, D. C. (2019). The role of aseismic slip in hydraulic fracturing-induced seismicity. *Science Advances*, *5*, eaav7172. https://doi.org/10.1126/sciadv.aav7172

Fang, Y., den Hartog, S. A. M., Elsworth, D., Marone, C., & Cladouhos, T. (2016). Anomalous distribution of microearthquakes in the Newberry Geothermal Reservoir: Mechanisms and implications. *Geothermics*, *63*, 62–73. https://doi.org/10.1016/j.geothermics.2015.04.005

Fang, Y., Elsworth, D., & Cladouhos, T. T. (2018). Reservoir permeability mapping using microearthquake data. *Geothermics*, *72*, 83–100. https://doi.org/10.1016/j.geothermics.2017.10.019

Fang, Y., Elsworth, D., Wang, C., Ishibashi, T., & Fitts, J. P. (2017). Frictional stability-permeability relationships for fractures in shales. *Journal of Geophysical Research: Solid Earth*, *122*, 1760–1776. https://doi.org/10.1002/2016JB013435

Fang, Y., Elsworth, D., Wang, C., & Jia, Y. (2018). Mineralogical controls on frictional strength, stability, and shear permeability evolution of fractures. *Journal of Geophysical Research: Solid Earth*, *123*, 3549–3563. https://doi.org/10.1029/2017JB015338

Faulkner, D. R., Sanchez-Roa, C., Boulton, C., & den Hartog, S. A. M. (2018). Pore fluid pressure development in compacting fault gouge in theory, experiments, and nature. *Journal of Geophysical Research: Solid Earth*, *123*, 226–241. https://doi.org/10.1002/2017JB015130

Garagash, D. I., & Germanovich, L. N. (2012). Nucleation and arrest of dynamic slip on a pressurized fault. *Journal of Geophysical Research*, *117*, B10310. https://doi.org/10.1029/2012JB009209

General Administration of Quality Supervision, Inspection and Quarantine of China (2003). *Determination of total organic carbon in sedimentary rock (GB/T 19145–2003)*. Beijing: Standards Press of China. [in Chinese]

Giorgetti, C., Carpenter, B. M., & Collettini, C. (2015). Frictional behavior of talc-calcite mixtures. *Journal of Geophysical Research: Solid Earth*, *120*, 6614–6633. https://doi.org/10.1002/2015JB011970

Gu, J. C., Rice, J. R., Ruina, A. L., & Tse, S. T. (1984). Slip motion and stability of a single degree of freedom elastic system with rate and state friction. *Journal of the Mechanics and Physics of Solids*, *32*(3), 167–196. https://doi.org/10.1016/0022-5096(84)90007-3

Guglielmi, Y., Cappa, F., Avouac, J. P., Henry, P., & Elsworth, D. (2015). Seismicity triggered by fluid injection-induced aseismic slip. *Science*, *348*(6240), 1224–1226. https://doi.org/10.1126/science.aab0476

Guo, T. (2013). Evaluation of highly thermally mature shale-gas reservoirs in complex structural parts of the Sichuan Basin. *Journal of Earth Science*, *24*(6), 863–873. https://doi.org/10.1007/s12583-013-0384-4

Hao, F., Zou, H., & Lu, Y. (2013). Mechanisms of shale gas storage: Implications for shale gas exploration in China. *AAPG Bulletin*, *97*(8), 1325–1346. https://doi.org/10.1306/02141312091

Hawkins, A. D., Xiao, S., Jiang, G., Wang, X., & Shi, X. (2017). New biostratigraphic and chemostratigraphic data from the Ediacaran Doushantuo formation in intra-shelf and upper slope facies of the Yangtze platform: Implications for biozonation of acanthomorphic acritarchs in South China. *Precambrian Research*, *300*, 28–39. https://doi.org/10.1016/j.precamres.2017.08.004

He, C., Tan, W., & Zhang, L. (2016). Comparing dry and wet friction of plagioclase: Implication to the mechanism of frictional evolution effect at hydrothermal conditions. *Journal of Geophysical Research: Solid Earth*, *121*, 6365–6383. https://doi.org/10.1002/2016JB012834

He, C., Yao, W., Wang, Z., & Zhou, Y. (2006). Strength and stability of frictional sliding of gabbro gouge at elevated temperatures. *Tectonophysics*, *427*(1–4), 217–229. https://doi.org/10.1016/j.tecto.2006.05.023

Ikari, M. J., Marone, C., & Saffer, D. M. (2011). On the relation between fault strength and frictional stability. *Geology*, *39*(1), 83–86. https://doi.org/10.1130/G31416.1

Inoue, A., & Utada, M. (1991). Smectite-to-chlorite transformation in thermally metamorphosed volcanoclastic rocks in the Kamikita area, northern Honshu, Japan. *American Mineralogist*, *76*(3–4), 628–640.

Jia, Y., Fang, Y., Elsworth, D., & Wu, W. (2019). Slip velocity dependence of friction-permeability response of shale fractures. *Rock Mechanics and Rock Engineering*, *53*(5), 2109–2121. https://doi.org/10.1007/s00603-019-02036-8

Jiang, S., Xu, Z., Feng, Y., Zhang, J., Cai, D., Chen, L., et al. (2016). Geologic characteristics of hydrocarbon-bearing marine, transitional and lacustrine shales in China. *Journal of Asian Earth Sciences*, *115*, 404–418. https://doi.org/10.1016/j.jseaes.2015.10.016

Ju, Y., Wang, G., Bu, H., Li, Q., & Yan, Z. (2014). China organic-rich shale geologic features and special shale gas production issues. *Journal of Rock Mechanics and Geotechnical Engineering*, *6*(3), 196–207. https://doi.org/10.1016/j.jrmge.2014.03.002

Kim, K. H., Ree, J. H., Kim, Y. H., Kim, S., Kang, S. Y., & Seo, W. (2018). Assessing whether the 2017 M_w 5.4 Pohang earthquake in South Korea was an induced event. *Science*, *360*(6392), 1007–1009. https://doi.org/10.1126/science.aat6081

King, G. C. P., Stein, R. S., & Lin, J. (1994). Static stress changes and the triggering of earthquakes. *Bulletin Seismological Society of America*, *84*(3), 935–953. https://doi.org/10.1016/0148-9062(95)94484-2

Kohli, A. H., & Zoback, M. D. (2013). Frictional properties of shale reservoir rocks. *Journal of Geophysical Research: Solid Earth*, *118*, 5109–5125. https://doi.org/10.1002/jgrb.50346

Leeman, J. R., Saffer, D. M., Scuderi, M. M., & Marone, C. (2016). Laboratory observations of slow earthquakes and the spectrum of tectonic fault slip modes. *Nature Communications*, *7*(1), 11104. https://doi.org/10.1038/ncomms11104

Lei, X., Huang, D., Su, J., Jiang, G., Wang, X., Wang, H., et al. (2017). Fault reactivation and earthquakes with magnitudes of up to M_w4. 7 induced by shale-gas hydraulic fracturing in Sichuan Basin, China. *Scientific Reports*, *7*, 7971. https://doi.org/10.1038/s41598-017-08557-y

Liang, C., Jiang, Z., Yang, Y., & Wei, X. (2012). Shale lithofacies and reservoir space of the Wufeng-Longmaxi formation, Sichuan Basin, China. *Petroleum Exploration and Development*, *39*(6), 736–743. https://doi.org/10.1016/S1876-3804(12)60098-6

Liang, C., Jiang, Z., Zhang, C., Guo, L., Yang, Y., & Li, J. (2014). The shale characteristics and shale gas exploration prospects of the Lower Silurian Longmaxi shale, Sichuan Basin, South China. *Journal of Natural Gas Science and Engineering*, *21*, 636–648. https://doi.org/10.1016/j.jngse.2014.09.034

Liu, S., Ma, W., Jansa, L., Huang, W., Zeng, X., & Zhang, C. (2013). Characteristics of the shale gas reservoir rocks in the Lower Silurian Longmaxi formation, East Sichuan Basin, China. *Energy Exploration and Exploitation*, *31*(2), 187–219. https://doi.org/10.1260/0144-5987.31.2.187

Logan, J. M., Dengo, C. A., Higgs, N. G., & Wang, Z. Z. (1992). Fabrics of experimental fault zones: Their development and relationship to mechanical behavior. In B. Evans, & T.-F. Wong (Eds.), *Fault mechanics and transport properties of rocks* (pp. 33–67). New York: Academic Press. https://doi.org/10.1016/S0074-6142(08)62814-4

Loucks, R. G., & Ruppel, S. C. (2007). Mississippian Barnett Shale: Lithofacies and depositional setting of a deep-water shale-gas succession in the Fort Worth Basin, Texas. *AAPG Bulletin*, *91*(4), 579–601. https://doi.org/10.1306/11020606059

Majer, E. L., Baria, R., Stark, M., Oates, S., Bommer, J., Smith, B., & Asanuma, H. (2007). Induced seismicity associated with enhanced geothermal systems. *Geothermics*, *36*(3), 185–222. https://doi.org/10.1016/j.geothermics.2007.03.003

Marone, C. (1998). Laboratory-derived friction laws and their application to seismic faulting. *Annual Review of Earth and Planetary Sciences*, *26*(1), 643–696. https://doi.org/10.1146/annurev.earth.26.1.643

Moore, D. E., & Lockner, D. A. (2004). Crystallographic controls on the frictional behavior of dry and water-saturated sheet structure minerals. *Journal of Geophysical Research*, *109*, B03401. https://doi.org/10.1029/2003JB002582

Moore, D. E., & Lockner, D. A. (2011). Frictional strengths of talc-serpentine and talc-quartz mixtures. *Journal of Geophysical Research*, *116*, B01403. https://doi.org/10.1029/2010JB007881

Moore, D. M., & Reynolds, R. C. Jr. (1989). *X-ray diffraction and the identification and analysis of clay minerals*. Oxford: Oxford University Press (OUP).

Mount, J. F. (1984). Mixing of siliciclastic and carbonate sediments in shallow shelf environments. *Geology*, *12*(7), 432–435. https://doi.org/10.1130/0091-7613(1984)12%3c432:MOSACS%3e2.0.CO;2

Pluymakers, A. M. H., Samuelson, J. E., Niemeijer, A. R., & Spiers, C. J. (2014). Effects of temperature and CO_2 on the frictional behavior of simulated anhydrite fault rock. *Journal of Geophysical Research: Solid Earth.*, *119*, 8728–8747. https://doi.org/10.1002/2014JB011575

Rankey, E. C. (2004). On the interpretation of shallow shelf carbonate facies and habitats: How much does water depth matter? *Journal of Sedimentary Research*, *74*(1), 2–6. https://doi.org/10.1306/071803740002

Rubinstein, J. L., & Mahani, A. B. (2015). Myths and facts on wastewater injection, hydraulic fracturing, enhanced oil recovery, and induced seismicity. *Seismological Research Letters*, *86*(4), 1060–1067. https://doi.org/10.1785/0220150067

Ruina, A. (1983). Slip instability and state variable friction laws. *Journal of Geophysical Research*, *88*(B12), 10,359–10,370. https://doi.org/10.1029/JB088iB12p10359

Saffer, D. M., Frye, K. M., Marone, C., & Mair, K. (2001). Laboratory results indicating complex and potentially unstable frictional behavior of smectite clay. *Geophysical Research Letters*, *28*(12), 2297–2300. https://doi.org/10.1029/2001GL012869

Sawai, M., Niemeijer, A. R., Plümper, O., Hirose, T., & Spiers, C. J. (2016). Nucleation of frictional instability caused by fluid pressurization in subducted blueschist. *Geophysical Research Letters*, *43*, 2543–2551. https://doi.org/10.1002/2015GL067569

Scuderi, M. M., & Collettini, C. (2016). The role of fluid pressure in induced vs. triggered seismicity: Insights from rock deformation experiments on carbonates. *Scientific Reports*, *6*, 24852. https://doi.org/10.1038/srep24852

Scuderi, M. M., & Collettini, C. (2018). Fluid injection and the mechanics of frictional stability of shale-bearing faults. *Journal of Geophysical Research: Solid Earth*, *123*, 8364–8384. https://doi.org/10.1029/2018JB016084

Segall, P., & Lu, S. (2015). Injection-induced seismicity: Poroelastic and earthquake nucleation effects. *Journal of Geophysical Research: Solid Earth*, *120*, 5082–5103. https://doi.org/10.1002/2015JB012060

Shapiro, S. A., Dinske, C., & Rothert, E. (2006). Hydraulic-fracturing controlled dynamics of microseismic clouds. *Geophysical Research Letters*, *33*, L14312. https://doi.org/10.1029/2006GL026365

Shen, L. W., Schmitt, D. R., & Schultz, R. (2019). Frictional stabilities on induced earthquake fault planes at Fox Creek, Alberta: A pore fluid pressure dilemma. *Geophysical Research Letters*, *46*, 8753–8762. https://doi.org/10.1029/2019GL083566

Stein, R. S. (1999). The role of stress transfer in earthquake occurrence. *Nature*, *402*(6762), 605–609. https://doi.org/10.1038/45144

Suckale, J. (2009). Induced seismicity in hydrocarbon fields. *Advances in Geophysics*, *51*, 55–106. https://doi.org/10.1016/S0065-2687(09)05107-3

Tan, J., Horsfield, B., Fink, R., Krooss, B., Schulz, H. M., Rybacki, E., et al. (2014). Shale gas potential of the major marine shale formations in the upper Yangtze platform, South China, part III: Mineralogical, lithofacial, petrophysical, and rock mechanical properties. *Energy & Fuels*, *28*(4), 2322–2342. https://doi.org/10.1021/ef4022703

Tembe, S., Lockner, D. A., & Wong, T.-F. (2010). Effect of clay content and mineralogy on frictional sliding behavior of simulated gouges: Binary and ternary mixtures of quartz, illite, and montmorillonite. *Journal of Geophysical Research*, *115*, B03416. https://doi.org/10.1029/2009JB006383

Vouillamoz, N., Wust Bloch, G. H., Abednego, M., & Mosar, J. (2016). Optimizing event detection and location in low-seismicity zones: Case study from western Switzerland. *Bulletin of the Seismological Society of America*, *106*(5), 2023–2036. https://doi.org/10.1785/0120160029

Walsh, F. R., & Zoback, M. D. (2015). Oklahoma's recent earthquakes and saltwater disposal. *Science Advances*, *1*, e1500195. https://doi.org/10.1126/sciadv.1500195

Wang, J. C., Shieh, C. F., & Chang, T. M. (2003). Static stress changes as a triggering mechanism of a shallow earthquake: Case study of the 1999 Chi-Chi (Taiwan) earthquake. *Physics of the Earth and Planetary Interiors*, *135*(1), 17–25. https://doi.org/10.1016/S0031-9201(02)00175-9

Wang, Y., Dong, D., Li, X., Huang, J., Wang, S., & Wu, W. (2015). Stratigraphic sequence and sedimentary characteristics of Lower Silurian Longmaxi formation in Sichuan Basin and its peripheral areas. *Natural Gas Industry B*, *2*(2–3), 222–232. https://doi.org/10.1016/j.ngib.2015.07.014

Xi, Y., Li, J., Liu, G., Cha, C., & Fu, Y. (2018). Numerical investigation for different casing deformation reasons in Weiyuan-Changning shale gas field during multistage hydraulic fracturing. *Journal of Petroleum Science and Engineering*, *163*, 691–702. https://doi.org/10.1016/j.petrol.2017.11.020

Xu, Z., Jiang, S., Yao, G., Liang, X., & Xiong, S. (2019). Tectonic and depositional setting of the Lower Cambrian and Lower Silurian marine shales in the Yangtze Platform, South China: Implications for shale gas exploration and production. *Journal of Asian Earth Sciences*, *170*, 1–19. https://doi.org/10.1016/j.jseaes.2018.10.023

Zhang, F., An, M., Zhang, L., Fang, Y., & Elsworth, D. (2019). The role of mineral composition on the frictional and stability properties of powdered reservoir rocks. *Journal of Geophysical Research: Solid Earth*, *124*, 1480–1497. https://doi.org/10.1029/2018JB016174

Zhang, F., Fang, Y., Elsworth, D., Wang, C., & Yang, X. (2017). Evolution of friction and permeability in a propped fracture under shear. *Geofluids*, *2017*, 2063747. https://doi.org/10.1155/2017/2063747

Zhang, L., & He, C. (2016). Frictional properties of phyllosilicate-rich mylonite and conditions for the brittle-ductile transition. *Journal of Geophysical Research: Solid Earth*, *121*, 3017–3047. https://doi.org/10.1002/2015JB012489

Zhou, J., Zhang, L., Li, X., & Pan, Z. (2019). Experimental and modeling study of the stress-dependent permeability of a single fracture in shale under high effective stress. *Fuel*, *257*, 116078. https://doi.org/10.1016/j.fuel.2019.116078

Ziv, A., & Rubin, A. M. (2000). Static stress transfer and earthquake triggering: No lower threshold in sight? *Journal of Geophysical Research*, *105*(B6), 13,631–13,642. https://doi.org/10.1029/2000jb900081

Zoback, M. D., & Gorelick, S. M. (2012). Earthquake triggering and large-scale geologic storage of carbon dioxide. *Proceedings of the National Academy of Sciences*, *109*(26), 10,164–10,168. https://doi.org/10.1073/pnas.1202473109

Zou, C., Dong, D., Wang, S., Li, J., Li, X., Wang, Y., et al. (2010). Geological characteristics and resource potential of shale gas in China. *Petroleum Exploration and Development*, *37*(6), 641–653. https://doi.org/10.1016/S1876-3804(11)60001-3

Zou, C., Dong, D., Wang, Y., Li, X., Huang, J., Wang, S., et al. (2016). Shale gas in China: Characteristics, challenges and prospects (II). *Petroleum Exploration and Development*, *43*(2), 182–196. https://doi.org/10.1016/S1876-3804(16)30022-2